Tectonics®

RESEARCH ARTICLE
10.1029/2022TC007662

Key Points:

- First ZHe and AHe data spanning the intracontinental Cathaysia Block
- Three-stage exhumation occurred in the intracontinental Cathaysia Block during Late Jurassic–Eocene times
- Regional thermochronological data favor significant exhumation triggered by the changing Paleo-Pacific Plate subduction processes

Supporting Information:

Supporting Information may be found in the online version of this article.

Correspondence to:

H. Li,
lihuan@csu.edu.cn

Citation:

Wu, J., Li, H., Danišík, M., Yonezu, K., Zheng, H., & Li, Z. (2023). Low-temperature thermochronological perspective on geodynamic evolution of the Cathaysia Block since Early Mesozoic. *Tectonics*, *42*, e2022TC007662. https://doi.org/10.1029/2022TC007662

Received 8 NOV 2022
Accepted 4 MAY 2023

Author Contributions:

Conceptualization: Jinghua Wu, Han Zheng
Formal analysis: Jinghua Wu
Funding acquisition: Jinghua Wu, Huan Li, Martin Danišík
Investigation: Jinghua Wu, Martin Danišík
Methodology: Jinghua Wu
Project Administration: Huan Li
Supervision: Huan Li, Kotaro Yonezu
Visualization: Jinghua Wu, Zhihan Li
Writing – original draft: Jinghua Wu
Writing – review & editing: Huan Li, Martin Danišík, Kotaro Yonezu

Low-Temperature Thermochronological Perspective on Geodynamic Evolution of the Cathaysia Block Since Early Mesozoic

Jinghua Wu[1,2], Huan Li[1], Martin Danišík[3], Kotaro Yonezu[2], Han Zheng[1], and Zhihan Li[1]

[1]Key Laboratory of Metallogenic Prediction of Nonferrous Metals and Geological Environment Monitoring, Ministry of Education, School of Geosciences and Info-Physics, Central South University, Changsha, China, [2]Department of Earth Resources Engineering, Faculty of Engineering, Kyushu University, Fukuoka, Japan, [3]John de Laeter Centre, Curtin University, Bentley, Australia

Abstract Mesozoic intrusive rocks are extensively outcropped in the Cathaysia Block (CB), indicating that they underwent significant exhumation after being formed. However, tectonothermal evolution of the CB during Mesozoic–Cenozoic times is still poorly constrained and associated geodynamic mechanisms driving the regional exhumation remain elusive. Toward this end, we present first zircon and apatite (U-Th)/He data of eight Mesozoic granitic plutons distributed across the intracontinental CB. Our new dating results are integrated with a compilation of regional low-temperature thermochronological data to determine the CB evolution in a tectonic and topographic evolution framework. Zircon and apatite (U-Th)/He central ages of the eight granitoids range from 146 to 30 and 82 to 31 Ma, respectively, implying a long-lasting exhumation of the intracontinental CB. Inverse thermal modeling of the thermochronological data for the eight plutons indicates that the intracontinental CB underwent three exhumation phases at 150–110, 110–85, and 66–38 Ma, of which the former two exhumation phases were prolonged and significant. A compilation of regional thermochronological data reveals a propagating locus of fast exhumation phase from the intracontinental CB to the seaward epicontinental CB over time. Combined with other geological evidence, we infer that primary exhumation events of the CB resulted from changing subduction processes of the Paleo-Pacific Plate, which include slab break-off and foundering in the Late Jurassic, progressive slab retreat in the Early Cretaceous, and normal subduction in the Late Cretaceous, with minor exhumation events presumably triggered by the Paleogene opening of the South China Sea Basin.

Plain Language Summary The Cathaysia Block (CB) is characterized by extensive outcrops of Mesozoic intrusive rocks. However, low-temperature thermochronological history of the CB, particularly in the far hinterland, is poorly constrained and variably interpreted. Consequently, geodynamic processes driving the remarkable crustal exhumation remain elusive. To address this issue, we report firsthand zircon and apatite (U-Th)/He dating results of eight Mesozoic granitoid plutons in the intracontinental CB and use these to unravel the detailed thermal history by applying inverse modeling. The integrated thermochronological data and inverse thermal history models indicate two major exhumation phases of the intracontinental CB in the Cretaceous, followed by a minor exhumation phase in the Paleogene. Further, regional thermochronological data were integrated into a map and spatiotemporal patterns over time were restored, enabling us to reconstruct a precise geochronological framework of regional exhumation events. The results reveal a migration locus of fast exhumation phase from the intracontinental CB to the seaward epicontinental CB over time. The propagating exhumation events, together with other geological observations, are explainable with advancing and retreating oceanic subduction processes. Therefore, we argue that the changing subduction processes were likely a primary inducement that set off significant tectonic and topographic changes of the CB.

1. Introduction

The Cathaysia Block (CB) underwent extensive magmatism, tectonism, and metallogeny during the Mesozoic (Cao et al., 2021; J. Li et al., 2014; Mao et al., 2013; Wu et al., 2023; Zhou et al., 2006). Despite numerous studies on the CB (Cao et al., 2021; Gao et al., 2017; Jiang et al., 2009; J. Li et al., 2014, 2017; Li, Dong, et al., 2016; Z. X. Li & Li, 2007; J. X. Liu et al., 2020; Mao et al., 2013; Shu et al., 2009; Suo et al., 2019; Zhou et al., 2006; Zhou & Li, 2000), long-standing debates remain as to geodynamic mechanisms driving the extensive

tectono-magmatic-metallogenic events, particularly in the Middle–Late Mesozoic. Proposed tectonic models explaining the CB evolution include Alps-type continental collision (Hsü et al., 1988), continental rifting due to multi-block interaction (Gilder et al., 1996; Y. J. Wang et al., 2008), and subduction of the Paleo-Pacific Plate. In addition, the assumptive oceanic subduction models vary in onset timing, durations, styles, and distances reached. The major oceanic subduction models include (a) changing-angle subduction from the Early Jurassic with the farthest reaching distance of ~800–1,000 km (Zhou & Li, 2000); (b) ~1,300 km flat-slab subduction since the Middle Permian (Li & Li, 2007); and (c) subduction initiated in the Jurassic and farthest reached the intracontinental CB with single or episodic slab advance, break-off and retreat (Jiang et al., 2009, 2015).

These tectonic models were established from magmatic, isotopic, structural, and sedimentary perspectives, and have succeeded in interpreting many of the geological observations in the CB. However, the evidence irreconcilable with the proposed models has been increasingly reported. For example, considerable structural analyses are not consistent with the Alps-type continental collision and continental rifting models, but indicative of the oceanic subduction model (Chu et al., 2019; Ji et al., 2018; J. Li et al., 2014). Some studies suggested that a lack of Triassic arc magmatism in the CB favors the onset of oceanic subduction later than the Triassic (Gao et al., 2017; Shu et al., 2008), seemingly inconsistent with much recent reports of Triassic arc-related magmatism in the epicontinental CB (Y. Wang et al., 2021b; Wei et al., 2021). Based on the variation of regional fission track ages, Y. J. Wang et al. (2020a) indicated that the subduction of the Paleo-Pacific Plate was restricted to the east of the Jiangnan Orogen rather than ~1,300 km slab subduction reaching to the Yangtze Block. A lack of clarity around the timing of Mesozoic tectonism has long vexed understanding of the CB tectonic evolution and caused a variety of interpretations. Therefore, a chronological characterization of the CB Mesozoic tectonism is prerequisite to determine the tectonic evolution as it can visualize spatiotemporal changes of tectonism and avoid being biased by local structures.

Mesozoic intrusive rocks crop out over an area of ~127,300 km^2 in the CB, implying a remarkable regional exhumation after the magma emplacement. As exhumation of intrusive rocks is commonly a crustal-scale response to plate tectonics, low-temperature thermochronology allows placing temporal constraints on the interplay between shallow and deep geological processes. However, low-temperature thermal history of the CB, particularly in the intracontinental regions, is not well documented and/or variably interpreted, making it difficult to assess the existing geodynamic models (Chen et al., 2020; Li, Shi, et al., 2016, 2017; Su et al., 2017; Sun et al., 2021; Y. J. Wang et al., 2020a). In addition, the tectonism and magmatism in the intracontinental CB are primarily Jurassic–Early Cretaceous in age whereas the epicontinental CB are more characterized by Late Cretaceous ages. Consequently, the previously suggested long-lived geodynamic processes (at least from the Early Jurassic to the Late Cretaceous) are poorly constrained in the intracontinental CB from the Jurassic onwards. Therefore, a comprehensive low-temperature thermochronological study of the CB is vital to resolution of these issues.

In this contribution, we present first zircon and apatite (U-Th)/He (ZHe and AHe, respectively) data of eight Mesozoic (mostly Late Jurassic) granitoid plutons laterally distributed across the intracontinental CB. Then, we reconstruct the thermal history using inverse modeling and compile all data into regional thermochronological maps to provide new insights into the tectonic and topographical evolution of the CB. Overarching goal of this study is to reveal exhumation history of intracontinental CB from the Early Mesozoic and to determine geodynamic mechanisms of regional exhumation.

2. Geological Setting

The South China Block (SCB) is flanked to the east by the Philippines Sea and Pacific Plates, to the north by the North China Craton, to the southwest by the Indochina Block, and to the west by the Tethyan–Himalayan Tectonic Belt (Figure 1a). During the Neoproterozoic Jiangnan Orogeny, the Yangtze and Cathaysia Blocks were amalgamated to form a rudiment of the SCB (Yao et al., 2019). The Jiangnan Orogen has been recognized as the suture zone, in part defined by the lithospheric-scale Jiangshan–Shaoxing and Anhua–Luocheng Faults. The northern margin of the Jiangnan Orogen is not clearly delineated by surface features (Figure 1a), and another southwestern margin is likely the Pingxiang–Guilin Fault despite much controversy (Shu et al., 2015). The Yangtze Block is characterized by northern Kongling Mesoarchean complexes, widespread Neoarchean basement, and varied Neoproterozoic magmatic rocks (Xia et al., 2012; Yu et al., 2012). In contrast, Precambrian rocks of the Cathaysia Block are mostly of Meso–Neoproterozoic age, with local outcrops of Paleoproterozoic rocks in the eastern region (e.g., Badu complexes; Cawood et al., 2018; Yao et al., 2019). Due to a vast expanse of the

10.1029/2022TC007662

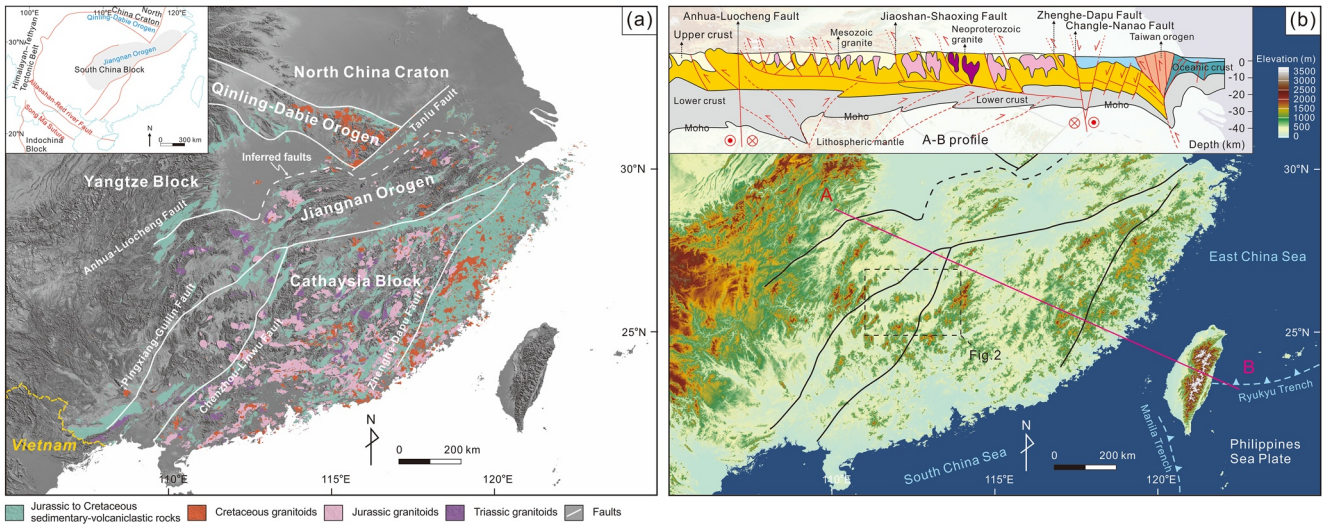

Figure 1. (a) Simplified geological map of South China (modified from Wang et al. (2013)); (b) 90 m digital elevation map of South China (http://www.gscloud.cn/home, A-B geological profile is modified from Li et al. (2019)).

SCB (~1,841,000 km^2), the Phanerozoic sedimentation, tectonism, and magmatism are varied in the eastern and western sides of the Anhua–Luocheng Fault, with the former tectonically influenced by multiple plates and the latter belonging to the Tethyan–Himalayan tectonic regime (Shu et al., 2008; Y. Wang et al., 2013). Phanerozoic tectono-magmatic events in the Jiangnan Orogen and Cathaysia Block include the Early Paleozoic intracontinental orogeny, Triassic continental collisions, and Jurassic–Cretaceous subduction of the Paleo-Pacific Plate, with ongoing debates around the timing and geodynamic mechanisms related to each (Gao et al., 2017; Shu et al., 2014, 2015). The Early Paleozoic orogeny was characterized by extensive absence of Silurian sedimentary rocks, greenschist facies metamorphism and deformation of pre-Silurian rocks, and granitoid-dominated magmatism (Shu et al., 2014; Song et al., 2015). The Triassic orogeny produced large-scale ductile shear deformation, thrust faults, folds, and granitoids, with locally developed medium- to high-grade metamorphism (Faure et al., 2016; Gao et al., 2017; Li, Dong, et al., 2016). The Jurassic–Cretaceous subduction gave rise to voluminous magmatism, intensive structural deformation, and massive polymetallic mineralization (e.g., W, Sn, Mo, Bi, Cu, Au, Pb, Zn, U, REEs, Nb, Ta, Rb, and Cs), which have been investigated for decades (Jiang et al., 2009; Li & Li, 2007; Mao et al., 2013; Shu et al., 2014, 2015; Y. Wang et al., 2013). Induced by multi-stage tectonism, the current topography of the CB exhibits as basin and range provinces (Figure 1b).

Mesozoic sedimentary rocks, mostly of Cretaceous age, are extensively distributed in the vicinity of Mesozoic granites across the CB (Figure 1a). Sediments are subdivided into four groups according to stratigraphic unconformities, including the Upper Triassic–Lower Jurassic strata, the Middle Jurassic strata, the Lower Cretaceous strata, and the Upper Cretaceous strata (C. Li et al., 2021; J. Li et al., 2014). The Upper Triassic–Lower Jurassic strata are fluvio–lacustrine facies and consist of conglomerates, sandstones, siltstones, and carbonaceous mudstones, with coal-bed intercalations (Shu et al., 2009). The Middle Jurassic strata are composed of fluvial-facies terrestrial clastic rocks (e.g., sandy gravels, sandstones, greywackes, and conglomerates) and bimodal volcanic rocks (e.g., basalts and rhyolites) (Shu et al., 2009). The Lower Cretaceous strata consist of a set of volcanic and sedimentary rocks that vary in lithology in the intracontinental and epicontinental CB, including siltstones, sandstones, mudstones, rhyolites, tuffs, and basaltic intercalations (J. Li et al., 2014; Y. Wang et al., 2013). The Upper Cretaceous strata comprise red-colored terrestrial clastic rocks such as sandstones, siltstones, mudstones, and a gypsum-bearing layer containing many fossils (Y. Wang et al., 2013). In addition, the Paleogene strata are also present and mainly composed of clastic rocks, siltstones, and mudstones, with intercalated gypsums and oil-bearing shales (C. Li et al., 2021; Shu et al., 2009).

Triassic tectonism of the CB is characterized by a lack of Middle Triassic strata, large-scale WNW-trending folds and thrusts, and local NE-striking ductile shear zones (Y. J. Wang et al., 2021a). These structures manifest NNE–SSW crustal shortening related to the Early Triassic continental collision between the SCB and the Indochina Block, followed by collision with the North China Craton (J. Li et al., 2017). The Jurassic to Cretaceous tectonism

includes NE/NNE-trending folds, thrusting/normal/strike-slip faults, and syn-tectonic extensional basins, which were interpreted as byproducts of oceanic subduction of the Paleo-Pacific Plate (J. Li et al., 2017).

Mesozoic magmatic rocks are widespread in the CB, with crystallization ages ranging from the Triassic to the Cretaceous. Triassic magmatic rocks in the CB are mostly I- and S-type granitoids, with minor A-type granitoids being identified in the epicontinental CB (Gao et al., 2017; Shu et al., 2015). These granitoids were emplaced throughout the Triassic, peaking at 240–220 Ma, and are primarily associated with multiple continental collisions between the SCB and other plates (Gao et al., 2017). In contrast, Jurassic magmatic rocks vary in lithology from felsic to mafic rocks, such as granites, syenites, granodiorites, granitic porphyries, diabases, and gabbros, with some bimodal volcanic rocks. Jurassic granitoids have been intensively studied and can be petrogenetically divided into I-, S-, and A-types as a result of remelting of inhomogeneous crustal basement with different degrees of mantle-derived contributions (C. Li et al., 2021; Y. Wang et al., 2003). Many Jurassic granitoids (particularly those of Middle to Late Jurassic age), have genetic relationships with nonferrous polymetallic mineralization. Jurassic mafic rocks are sparsely distributed and include two groups with asthenospheric-mantle-derived and lithospheric-mantle-derived origins (Meng et al., 2012; Y. Wang et al., 2003). The latter were sourced from an enriched mantle that was metasomatized by slab-released fluids/melts, indicative of a potential onset of oceanic subduction in the Jurassic (Meng et al., 2012). Cretaceous magmatic rocks, typified by intensive arc-related rocks in the epicontinental CB, have been related to the subduction of the Paleo-Pacific Plate. They share the similar lithology with Jurassic magmatic rocks but progressively show strong arc signatures over time. Chronologically, they were emplaced from 145 to 85 Ma, with two peak episodes at ∼132 and ∼98 Ma (C. Li et al., 2021).

3. Sampling and Analytical Methods

Zircon and apatite (U-Th)/He analyses were conducted on eight Mesozoic granitoid plutons in the intracontinental SCB, constituting a lateral transect across the intracontinental CB (Figure 2). For some individual granitoid plutons, samples were collected to constitute a steep elevation profile, including the Tongshanling, Baoshan, Qitianling, and Wangxianling plutons. Detailed sample locations and information are summarized in Table 1.

3.1. Zircon and Apatite (U-Th)/He Dating

Mineral separation was carried out in the Rock–Mineral Preparation Lab, Central South University. The whole rock samples were crushed using a ball mill, sieved to 75–200 μm fraction and separated for heavy minerals using a table concentrator. Many granitoids in this study are highly evolved A-type granites, with low phosphorous contents (Kong et al., 2018). These P-unsaturated melts do not facilitate apatite precipitation and apatite grains were separated from four granitoid plutons only.

(U-Th)/He dating of apatite and zircon was conducted in the Western Australia Thermo-Chronology Hub (WATCH) Facility, John de Laeter Centre (Curtin University) and followed the procedures detailed in Danišík et al. (2012, 2017). Euhedral zircon and apatite grains were selected and carefully examined under a high-power microscope. Euhedral inclusion-free zircon and apatite crystals were loaded into niobium and platinum microtubes, respectively. An Alphachron MK II system (Australian Scientific Instruments, ASI) equipped with a 970 nm diode laser was used to extract ^{4}He from mineral grains at temperature of 960°C held for 5 min (apatite) or 1,250°C held for 15 min (zircon). This process was repeated to ensure total extraction of radiogenic ^{4}He. ^{4}He content was determined by isotope dilution using a quadrupole mass spectrometer (Prisma Plus QMG 220).

After the ^{4}He extraction, apatite and zircon crystals were dissolved according to the procedure of Evans et al. (2005). For apatite, 25 μL of spike solution ^{235}U and ^{230}Th was added to the vials which were ultrasonicated for 15 min and then left for ∼4 hr at room temperature to ensure complete dissolution. A total of 450 μl of Milli-Q water was added to dilute the solutions for U-Th-Sm analysis on an Element XR™ High Resolution inductively coupled plasma-mass spectrometer (ICP-MS). Zircon was spiked with 25 μL of ^{235}U and ^{230}Th spike solution and dissolved in 350 μL of HF using Parr bombs heated to 220°C for 48 hr. Once the Parr bombs cooled to room temperature, the vials were placed on a hot plate at 70°C for ∼48 hr to evaporate the HF and enable the precipitation of fluoride salts. Consequently, 300 μL and 9 mL of HCl were added to the Parrish vials and the liner, respectively, which were then returned to the Parr bombs and heated at 200°C for 24 hr. The solutions were then evaporated down to 50 μL, diluted with 600 μL of Milli-Q water, and then transferred to 2 mL conical-base plastic vials, ready for U-Th analysis on ICP-MS.

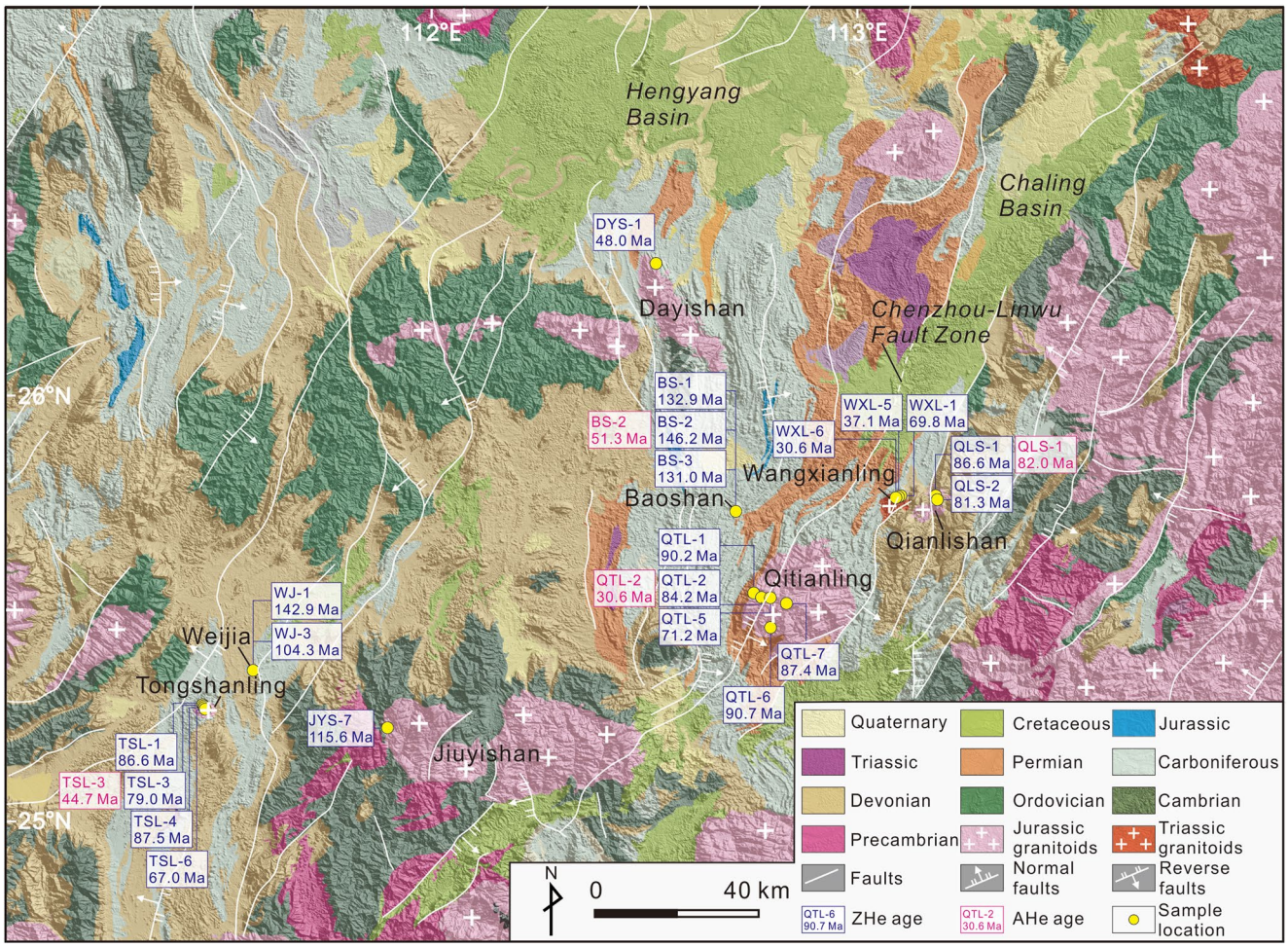

Figure 2. Geological map of the investigated area (https://geocloud.cgs.gov.cn).

Mineral age standards including Fish Canyon zircon (28.3 ± 2.6 Ma; Reiners, 2005) and Durango apatite (31.5 ± 1.0 Ma; Evans et al., 2005) were used to monitor accuracy of the analytical procedure. Weighted mean (U-Th)/He dates of 28.5 ± 0.5 Ma ($n = 9$) and 31.2 ± 0.7 Ma ($n = 7$) Ma obtained for the Fish Canyon zircon and Durango apatites, respectively, are consistent with the recommended values within error (Table S1 in Supporting Information S1).

Isoplot R (Vermeesch, 2018) and Helioplot 2.0 (Vermeesch, 2010) programs were used to generate weighted mean age and central age for the obtained ZHe or AHe dates. A pilot calculation of central age using all the ZHe or AHe dates of each granitoid sample was performed. Weighted mean age and central age were recalculated after rejecting anomalous ages that led to high dispersion (>15%) of the raw central age, with the cause of dispersion discussed below. As a result, weighted mean ages and central ages of all samples are identical within error. The central age was further used for inverse thermal modeling and following interpretation as it is the most accurate representation of the average age in single-sample analyses (Vermeesch, 2008).

3.2. Inverse Thermal Modeling

Inverse thermal modeling was performed using HeFTy v1.9.0 (Ketcham, 2005) and QTQt V5.4.6 (Gallagher, 2012) programs. The two programs run with different inverse modeling algorithms (Vermeesch & Tian, 2014) and the results are combined in this work to derive a more complete thermal history. Due to different sampling strategies during the fieldwork, methods of inverse thermal modeling are varied for each pluton, including multi-minerals, elevation profile, and single zircon constraint methods (Table 2). Specifically, multi-minerals constraint method

Table 1
Sample Information

Sample no.	Lithology	Elevation (m)	Latitude and longitude	Emplacement age (Ma)
TSL-1	Granodiorite	638	25.2750°N, 111.4619°E	166.6 ± 0.4 Ma
TSL-3	Granodiorite	723	25.2722°N, 111.4644°E	(MSWD = 0.23)
TSL-4	Granodiorite	823	25.2689°N, 111.4656°E	Kong et al., 2018
TSL-6	Granodiorite	904	25.2650°N, 111.4675°E	
WJ-1	Granite porphyry	295	Borehole of the Weijia deposit 25.3558°N, 111.5806°E	158.7 ± 2.3 Ma
				(MSWD = 0.78)
WJ-3	Granite porphyry	195		Kong et al., 2018
JYS-7	Granite	1,028	25.2211°N, 111.8953°E	153.0 ± 0.9 Ma
				(MSWD = 0.18)
				Y. Liu et al., 2019
DYS-1	Granite	143	26.3193°N, 112.5356°E	158.2 ± 1.2 Ma
				(MSWD = 1.2)
				R. Zhang et al., 2021
BS-1	Granodioritic porphyry	−150	Underground tunnels of the Baoshan deposit 25.7300°N, 112.7144°E	167.0 ± 3.0 Ma
BS-2	Granodioritic porphyry	−270		(MSWD = 1.12)
				Kong et al., 2018
BS-3	Granodioritic porphyry	−110		
QTL-1	Granite	684	25.5381°N, 112.7564°E	157 ± 3 Ma
QTL-2	Granite	1,016	25.5275°N, 112.7753°E	(MSWD = 0.68)
QTL-5	Granite	1,161	25.5269°N, 112.7961°E	Zhu et al., 2009
QTL-6	Granite	1,346	25.5136°N, 112.8342°E	
QTL-7	Granite	605	25.4567°N, 112.7967°E	
WXL-1	Granite	319	25.7744°N, 113.1339°E	223.5 ± 1.8 Ma
WXL-5	Granite	388	25.7708°N, 113.1042°E	(MSWD = 0.29)
WXL-6	Granite	420	25.7706°N, 113.1019°E	R. Q. Zhang et al., 2015
QLS-1	Granite	276	25.7672°N, 113.1619°E	155 ± 2 Ma
QLS-2	Granite	347	25.7575°N, 113.1657°E	(MSWD = 1.19)
				Shu et al., 2011

refers to using ZHe and AHe data from the same sample to perform inverse thermal modeling. Elevation profile and single zircon constraint methods were applied to topography with and without significant altitudinal changes, respectively. In addition, individual zircon/apatite grains that yielded a similar age to the central age of the host-sample were selected for inverse modeling. Detailed inverse modeling strategies for each pluton are shown in Table 2.

When performing QTQt inverse modeling, we set the present temperature and geothermal gradient as 10 ± 10°C and 30 ± 10 C/km, respectively. All the modeling processes run with 100,000 iterations for burn-in process and 100,000 for posterior ensemble, with no obvious trend in the likelihood/posterior chain for all models. For the HeFTy inverse modeling, the software-designed present temperature (20°C) was adopted. As HeFTy does not work well with too many sample constraints (Vermeesch & Tian, 2014), single zircon/apatite grain of each granitoids was selected to the inverse modeling and presented in Table 2. A Monte Carlo method was used to run 20,000 paths for each granitoid during the HeFTy inverse modeling. All the raw input files can be accessed at https://data.mendeley.com/drafts/vpgcdwn569.

Based on published thermochronological data of these granitoids (Table 2), zircon U-Pb ages of the investigated granitoids (Table 1), zircon U-Pb closure temperature (950 ± 50°C; Cherniak & Watson, 2001), molybdenite

Table 2
Inverse Modeling Strategies for the Investigated Plutons

	(U-Th)/He age span (Ma)		Samples for inverse modelling		
Samples	Zircon	Apatite	Zircon	Apatite	Time-temperature constraints
Tongshanling	56–93	37–60	TSL3-3	TSL3-6	950 ± 50℃ and 167 ± 1 Ma
			(Multi-minerals for QTQt)		520 ± 20℃ and 162 ± 2 Ma
			TSL3-3	TSL3-6	(Mol. Re-Os age, Zhao et al., 2016)
			(Multi-minerals for HeFTy)		
					180 ± 20℃ and 75 ± 25 Ma
					70 ± 20℃ and 50 ± 15 Ma
Weijia	83–162		WJ1-3		950 ± 50℃ and 159 ± 2 Ma
			WJ3-4		520 ± 20℃ and 159 ± 6 Ma
			(Vertical profile for QTQt)		(Mol. Re-Os age, Zhao et al., 2016)
			WJ1-3		
			(Single zircon for HeFTy)		180 ± 20℃ and 120 ± 45 Ma
Jiuyishan	97–141		JYS7-5		950 ± 50℃ and 153 ± 1 Ma
			(Single zircon for QTQt)		520 ± 20℃ and 151 ± 2 Ma
			JYS7-5		(Mol. Re-Os age Fu et al., 2007)
			(Single zircon for HeFTy)		
					180 ± 20℃ and 120 ± 25 Ma
Dayishan	44–56		DYS1-4		950 ± 50℃ and 158 ± 1 Ma
			(Single zircon for QTQt)		350 ± 50℃ and 150 ± 1 Ma
			DYS1-4		(Mus. ^{39}Ar-^{40}Ar age Lu et al., 2021)
			(Single zircon for HeFTy)		
					180 ± 20℃ and 50 ± 10 Ma
Baoshan	116–148	42–63	BS2-6	BS2-4	950 ± 50℃ and 167 ± 3 Ma
			(Multi-minerals for QTQt)		520 ± 20℃ and 160 ± 2 Ma
			BS2-6	BS2-4	(Mol. Re-Os age Lu et al., 2006)
			(Multi-minerals for HeFTy)		
					180 ± 20℃ and 130 ± 20 Ma
					70 ± 20℃ and 50 ± 15 Ma
Qitianling	64–103	26–36	QTL2-1	QTL2-1	950 ± 50℃ and 157 ± 3 Ma
			(Multi-minerals for QTQt)		350 ± 50℃ and 158 ± 0.3
			QTL2-1	QTL2-1	Ma (Mus. ^{39}Ar-^{40}Ar age Mao et al., 2004)
			(Multi-minerals for HeFTy)		
					180 ± 20℃ and 85 ± 25 Ma
					70 ± 20℃ and 30 ± 10 Ma
Wangxianling	28–82		WXL1-1		950 ± 50℃ & 224 ± 2 Ma
			WXL5-5		350 ± 50℃ and 214 ± 1 Ma
			WXL6-3		(Mus. ^{39}Ar-^{40}Ar age R. Q. Zhang et al., 2015)
			(Vertical profile for QTQt)		
			WXL5-5		180 ± 20℃ and 55 ± 30 Ma
			(Single zircon for HeFTy)		

Table 2
Continued

Samples	(U-Th)/He age span (Ma)		Samples for inverse modelling		Time-temperature constraints
	Zircon	Apatite	Zircon	Apatite	
Qianlishan	77–96	75–89	QLS1-4	QLS1-3	950 ± 50℃ and 155 ± 2 Ma
			(Multi-minerals for QTQt)		350 ± 50℃ and 151 ± 1 Ma
			QLS1-4	QLS1-3	(Mus. ^{39}Ar-^{40}Ar age Zhao et al., 2018)
			(Multi-minerals for HeFTyt)		180 ± 20℃ and 85 ± 15 Ma

Re-Os ages of granitoid-related ores, molybdenite Re-Os closure temperature (520 ± 20°C; Suzuki et al., 1996; Chew & Spikings, 2015), ^{39}Ar/^{40}Ar ages of muscovite, argon closure temperatures of muscovite (350 ± 50°C; Hames & Bowring, 1994), helium closure temperatures of zircon and apatite (180 ± 20 and 70 ± 20°C, respectively; Wolf et al., 1996; Reiners et al., 2002, 2004), and a slightly larger He age span of each pluton (e.g., 75 ± 25 for 56–93 Ma of the Tongshanling pluton) were adopted as initial time-temperature (t-T) constraints for QTQt and HeFTy inverse modeling processes (Table 2). Paleo-geothermal gradient is assumed at 25 ± 5°C to estimate exhumation rate.

3.3. Synthesis of Regional Magmatism and Thermochronological Data

We collected geochronological data and latitude-longitude coordinates of Mesozoic magmatism to map their spatiotemporal patterns for further discussion. Histogram and kernel density estimation were used to roughly divide the Mesozoic magmatism into different age groups. To detail the spatial variation in the Mesozoic magmatism, we calculate relative distances of the Mesozoic magmatic rocks away from a presumptive orogen-parallel line (mathematically expressed as $-X + Y + 97 = 0$ based on Cartesian coordinates, where X and Y are longitude and latitude in degree, respectively). The K-means clustering analysis was ultimately used to precisely group the Mesozoic magmatic rocks according to their ages and relative distances.

In addition, reported low-temperature thermochronological data from the CB and Jiangnan Orogen, including zircon fission track (ZFT), ZHe, apatite fission track (AFT), and AHe ages, are compiled to map their spatiotemporal patterns for a better understanding of regional tectonothermal evolution. To evaluate a potential influence of thermal resetting on these low-temperature thermochronological data, the relative distances between these samples and a datum point (105°E, 20°N) are calculated using Cartesian coordinates (in degrees).

4. Results

A total of 102 ZHe and 23 AHe ages from 21 granitoid samples are summarized in Tables S2 and S3 in Supporting Information S1, respectively.

4.1. Zircon (U-Th)/He Data

For Tongshanling granodiorite samples (n = 4), a total of 16 zircon grains yield ZHe dates (F_T-corrected age, the same below) ranging from 56.0 ± 3.1 to 93.4 ± 5.1 Ma (1 sigma error), with four dispersed ZHe dates older than 130 Ma (Figure 3a). For Weijia granite porphyry samples (n = 2), 6 ZHe dates were obtained and vary from 83.2 ± 4.6 to 162.7 ± 16.8 Ma, with four significantly dispersed ZHe dates (>180 Ma) (Figure 3b). For one Jiuyishan granite sample, five ZHe dates are between 97.0 ± 5.3 Ma and 141.0 ± 14.5 Ma (Figure 3c). For one Dayishan granite sample, 3 ZHe dates show a narrow range of 43.6 ± 2.4 to 56.2 ± 3.2 Ma, with two dispersed ZHe dates of 74.2 ± 4.0 and 97.0 ± 5.3 Ma (Figure 3d). For Baoshan granodioritic samples (n = 3), 11 zircon grains were dated between 115.9 ± 6.4 and 148.4 ± 8.0 Ma, with two young dispersed ZHe dates of 70.3 ± 3.8 and 84.6 ± 4.7 Ma (Figure 3e). For Qitianling granite samples (n = 5), 24 ZHe dates vary from 64.3 ± 3.5 to 103.3 ± 5.7 Ma and one zircon grain yields an anomalously old ZHe date of 248.9 ± 13.6 Ma (Figure 3f). For Wangxianling granite samples (n = 3), 13 zircon grains give variable ZHe dates ranging from 28.3 ± 1.5 to 82.4 ± 4.4 Ma and two zircon grains produce dispersed ZHe dates of 17.2 ± 0.9 and 52.1 ± 2.9 Ma

10.1029/2022TC007662

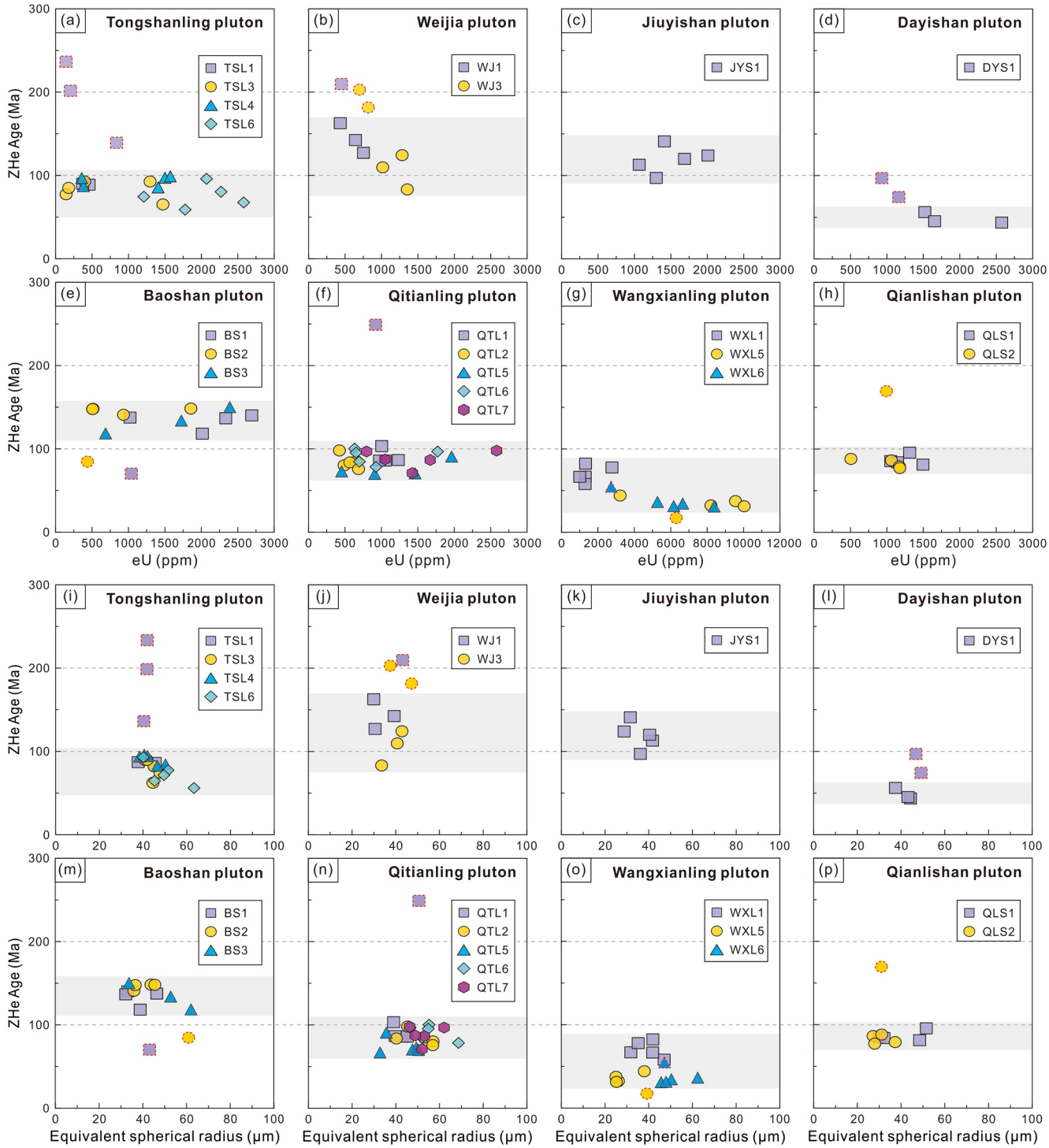

Figure 3. Plots of (a–h) eU versus ZHe date and (i–p) equivalent spherical radius (ES radius) versus ZHe date for different plutons in the studied area. Dispersed samples are marked with the red dash line.

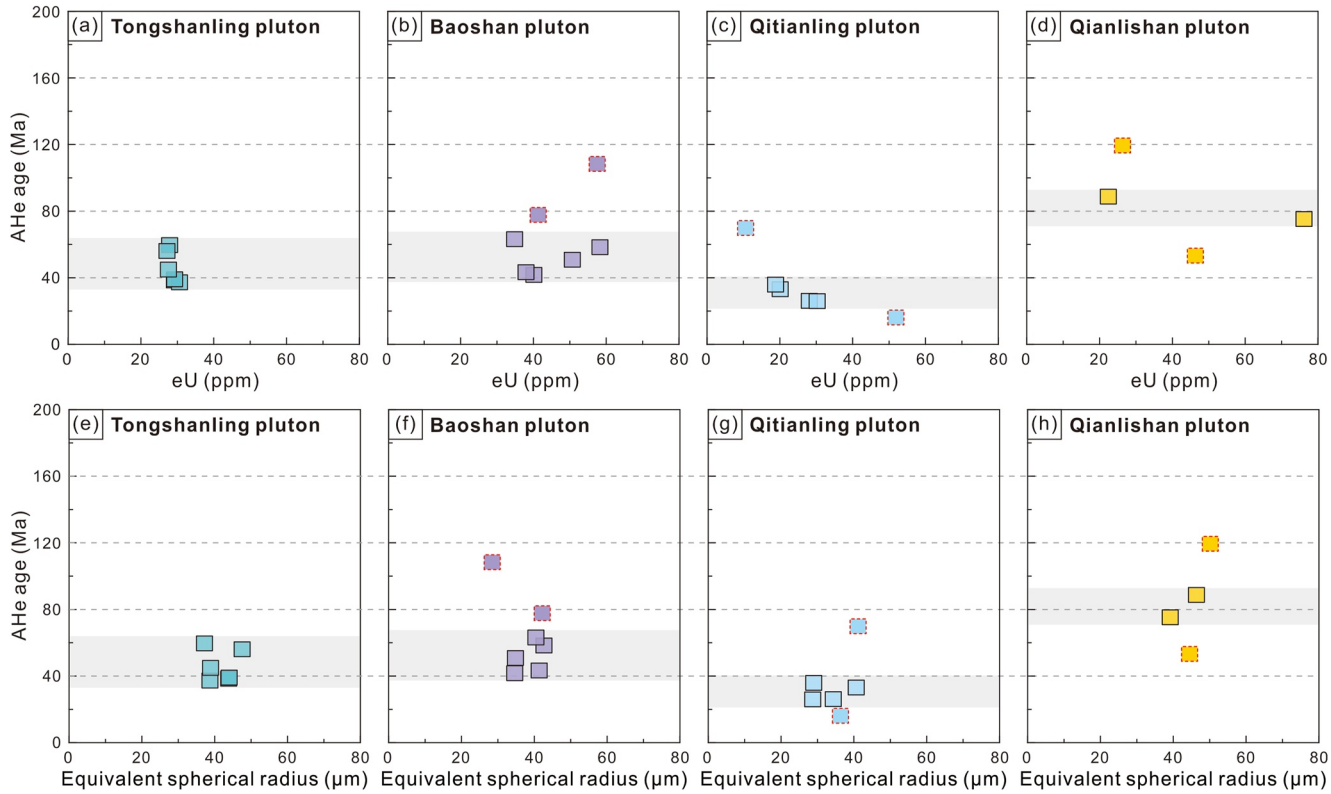

Figure 4. Plots of (a–d) eU versus AHe date and (e–h) equivalent spherical radius (ES radius) versus AHe date for different plutons in the studied area. Dispersed samples are marked with the red dash line.

(Figure 3g). For Qianlishan granite samples ($n = 2$), 8 zircon grains generate ZHe dates ranging from 77.2 ± 7.9 to 95.6 ± 5.2 Ma with one dispersed sample (QLS2-5) of 169.5 ± 17.3 Ma (Figure 3h).

4.2. Apatite (U-Th)/He Data

For one Tongshanling granodiorite sample, 6 apatite grains yield AHe dates ranging from 37.3 ± 2.5 to 59.6 ± 6.3 Ma (Figure 4a). For one Baoshan granodioritic sample, 5 apatite grains give AHe dates between 41.7 ± 4.5 and 63.2 ± 4.1 Ma, with two dispersed AHe dates of 77.7 ± 4.7 and 108.3 ± 16.9 Ma (Figure 4b). For one Qitianling granite sample, five apatite grains generate AHe dates of 41.7 ± 4.5 to 63.2 ± 4.1 Ma, with two dispersed AHe dates of 16.1 ± 1.7 and 69.9 ± 4.5 Ma (Figure 4c). For one Qianlishan granite sample, two apatite grains yield AHe dates of 75.3 ± 5.1 to 88.7 ± 5.7 Ma, with two dispersed samples (QLS1-2 and QLS1-5) of 53.3 ± 3.2 to 119.4 ± 7.1 Ma (Figure 4d).

4.3. Thermal History Modeling Results

The HeFTy model shows that Tongshanling pluton experienced a three-step cooling: (a) rapid cooling at 167–164 Ma and gradual cooling at 164–102 Ma; (b) quick cooling at 102–93 Ma and steady cooling at 93–62 Ma; and (c) rapid cooling at 62–55 Ma and slow cooling to the surface since 55 Ma (Figure 5a). The QTQt model indicates a similar three-step thermal history of Tongshanling pluton with fast cooling at 167–161 Ma, moderate cooling at 161–100 Ma, rapid cooling across the ZHe partial retention zone (ZPRZ) at 100–97 Ma, residence in the AHe partial retention zone (APRZ) at 97 to 65 Ma, and rapid cooling to surface temperature at 65–61 Ma (Figure 5e).

The HeFTy model deciphers a two-phase cooling history for Weijia pluton, with a rapid cooling occurring at 160–149 Ma and gradual cooling since 149 Ma (Figure 5b). Similarly, the QTQt model shows that Weijia pluton underwent rapid cooling at 161–158 Ma, followed by a decrease in cooling rate since 158 Ma (Figure 5f).

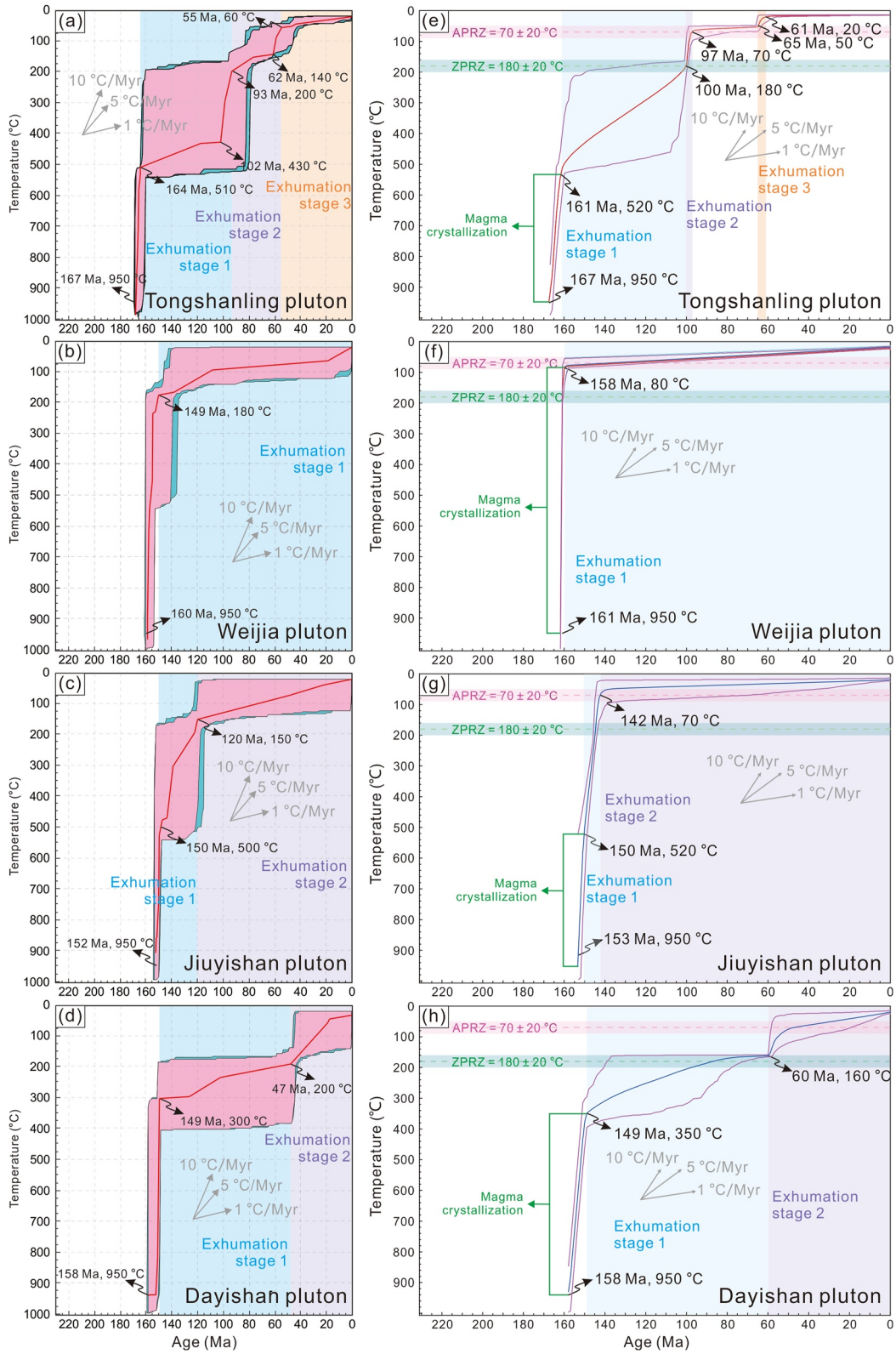

Figure 5. Inverse modeling T-t pathways of (a–d) HeFTy program and (e–h) QTQt program for the studied granitoids in the west of Chenzhou–Linwu Fault.

Similar to Weijia pluton, both the HeFTy and QTQt models show a two-phase thermal history for Jiuyishan pluton: rapid cooling at 153–120 Ma (HeFTy model, Figures 5c) and 153–142 Ma (QTQt model, Figure 5g), with further slow cooling since 120 Ma (HeFTy model) and 142 Ma (QTQt model).

The HeFTy model shows that Dayishan pluton experienced ~9 Myr of rapid cooling since 158 Ma, moderate cooling at 149–47 Ma, and accelerated cooling since 47 Ma (Figure 5d). In contrast, the QTQt models suggests fast cooling at 158–149 Ma and moderate cooling from 149 Ma to 60 Ma, with gradual cooling to the surface since 60 Ma (Figure 5h).

Baoshan pluton experienced a three-stage thermal history as revealed by the two inverse models: rapid cooling (168–140 Ma of HeFTy model vs. 168–148 Ma of QTQt model), long residence in APRZ (140–62 Ma of HeFTy model vs. 148–66 Ma of QTQt model), and a rapid cooling to the surface in the Paleogene (62–44 Ma of HeFTy model vs. 66–63 Ma of QTQt model) (Figures 6a and 6e).

A four-step thermal history is observed in Qitianling pluton which experienced a rapid cooling in the Late Jurassic (159–158 Ma of HeFTy model vs. 160–157 Ma of QTQt model), a moderate cooling until close to the Early Cretaceous (158–114 Ma of HeFTy model with 114–74 Ma quiescence vs. 157–110 Ma of QTQt model), an accelerated cooling to ~60°C (74–55 Ma of HeFTy model vs. 110–100 Ma of QTQt model), long residence at APRZ (55–28 Ma of HeFTy model vs. 100–41 Ma of QTQt model), and further rapid cooling to the surface (28–0 Ma of HeFTy model vs. 41–35 Ma of QTQt model) (Figures 6b and 6f).

Wangxianling pluton experienced a complex cooling history since the Middle Triassic (~225 Ma) as illustrated the HeFTy model (Figure 6c): (a) an remarkable cooling from 222 to 216 Ma, (b) an inconstant cooling during 216–35 Ma, and (c) a fast cooling to the surface since 35 Ma. In comparison, the QTQt model indicates a six-phase cooling history which includes rapid cooling at 225–213 Ma, long-lived residual at 213–133 Ma, accelerated cooling at 133–82 Ma, residual in ZPRZ at 82–59 Ma, short-lived fast cooling (59–56 Ma), and steady cooling to the surface since 56 Ma (Figure 6g).

As shown in the HeFTy model (Figure 6d), Qianlishan pluton underwent fast cooling and moderate cooling at 157–150 and 150–100 Ma, respectively, resided in the ZPRZ at 100–82 Ma, and reached the shallow surface at 82–78 Ma, with slow cooling to the surface since 78 Ma. The QTQt models indicate a fast cooling at 156–146 Ma, gradual cooling at 146–125 Ma, 125–100 Ma residence in the ZPRZ, and two-step accelerated cooling to the surface at 100–86 Ma (Figure 6h).

4.4. Spatiotemporal Patterns of the Mesozoic Magmatism

Spatially, Mesozoic magmatic rocks are mostly distributed within the CB, with minor located in the Jiangnan Orogen (Figures 7a and 7d and Figure S1 in Supporting Information S1). Chronologically, the histogram and kernel density estimation (KDE) curve (Figure 7e) illustrate that four episodic Mesozoic magmatism occurred in the CB and peaked at the Late Triassic (230 Ma), Late Jurassic (158 Ma), Early Cretaceous (132 Ma), and Late Cretaceous (97 Ma), respectively. Based on the K-means clustering analysis, four detailed age clusters of the Mesozoic magmatism are recognized (i.e., episode 1 of 256–202 Ma, episode 2 of 195–147 Ma, episode 3 of 146–117 Ma, and episode 4 of 116–86 Ma; Figure 7f).

Chronological mapping of the Mesozoic magmatic rocks reveals a systematical spatiotemporal pattern: (a) in the Triassic, magmatism mostly occurred in the intracontinental CB (with distance mostly >500 km) (Figure 7f and Figure S1 in Supporting Information S1); (b) in the Early Jurassic, magmatism increased from the sub-epicontinental to the intracontinental CB, peaking in the Late Jurassic (~155–160 Ma) (Figures 7b and 7f); (c) in the Early Cretaceous, magmatism intensified again in the intracontinental CB and trended to the margin over time, with numerous magmatic rocks intensively distributed in the eastern Jiangnan Orogen (Figures 7c and 7f); and (d) massive magmatism migrated to the epicontinental CB during the Late Cretaceous (Figures 7d and 7f).

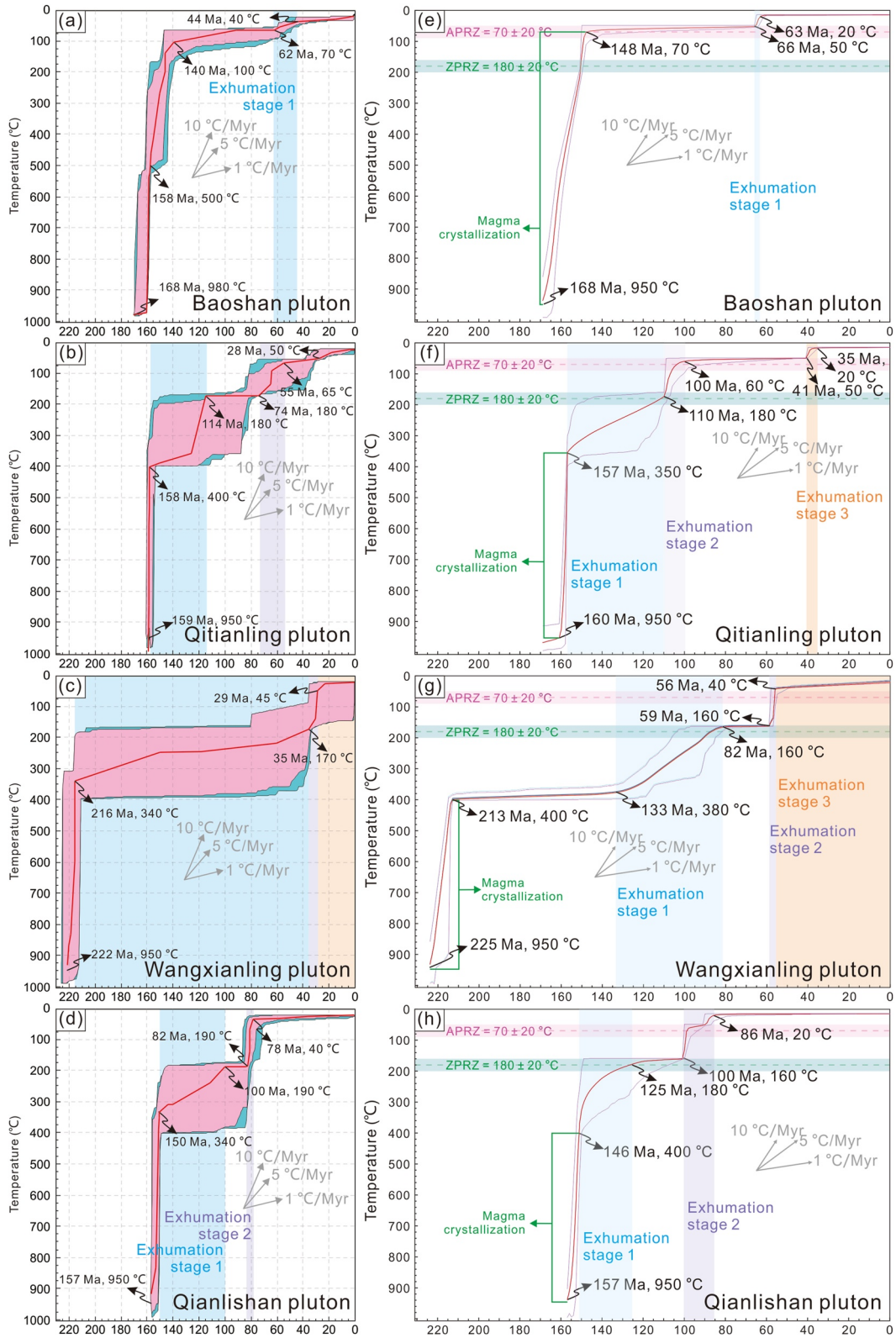

Figure 6. Inverse modeling T-t pathways of (a–d) HeFTy program and (e–h) QTQt program for the studied granitoids in the east of Chenzhou–Linwu Fault.

10.1029/2022TC007662

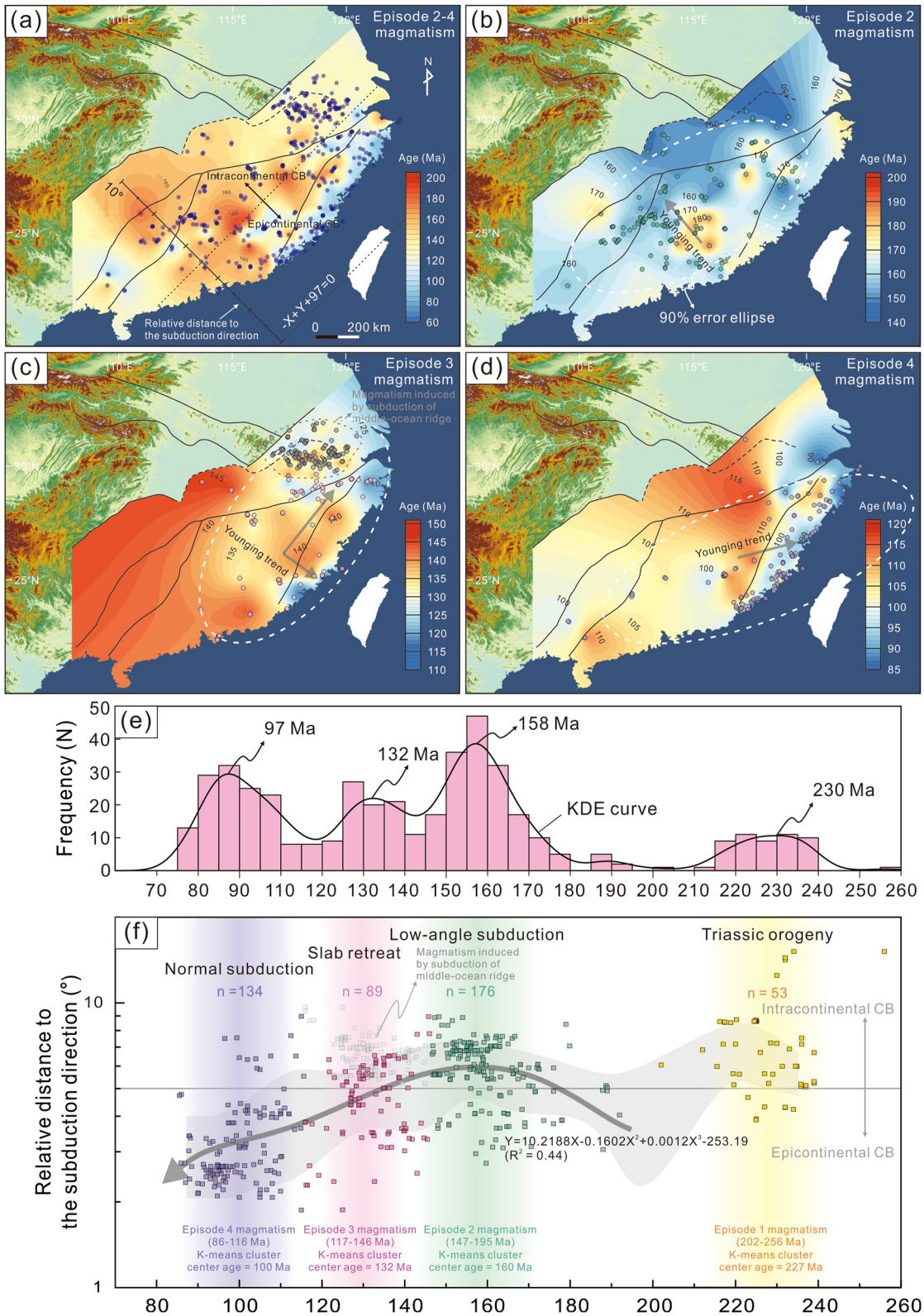

Figure 7. Contour maps showing the distribution and age variation of (a) Jurassic to Cretaceous magmatism, (b) episode 2 magmatism, (c) episode 3 magmatism, and (d) episode 4 magmatism in the CB and Jiangnan Orogen (Data source: Liu et al., 2020; dark blue, green, pink, and violet points are locations of episodes 2–4, episode 2, episode 3, and episode 4 magmatic rocks, respectively); (e) frequency histogram showing age clusters of the Mesozoic magmatism in the Cathaysia Block and Jiangnan Orogen; and (f) magmatic age versus relative distance to the subduction plot showing the spatiotemporal change of the Mesozoic magmatism in the Cathaysia Block and Jiangnan Orogen (gray error margin is calculated based on every 10 Myr magmatism from 80 Ma).

5. Discussion

5.1. Assessment and Interpretation of the (U-Th)/He Data

As shown in the results (Tables S2 and S3 in Supporting Information S1), many samples show a wide intrasample variation of ZHe/AHe ages and which may be related to crystal sizes, U-Th-rich inclusions, U-Th zonation, and radiation damage in individual crystal grains (Brown et al., 2013; Guenthner et al., 2013; Reiners & Farley, 2001; Willett et al., 2017).

Helium retention and closure temperature are elevated as the intensity of radiation damage increases (Flowers et al., 2007; Gautheron et al., 2009; Shuster et al., 2006). The damage can be numerically estimated by eU values (concentrations of effective U, defined as $eU = U + 0.235 \times Th$ in ppm). In this study, the eU values do not correlate with ZHe/AHe ages, indicating that radiation damage was not the critical control on anomalously old He ages (Figures 3a–3h and 4a–d). In addition, most analyzed zircon/apatite crystals were of comparable size and no positive correlation of ZHe/AHe ages and grain radii is noted (Figures 3i–3p and 4e–4h). This suggests grain sizes are not responsible for the anomalously old He ages.

Zircon and apatite grains with U-Th-enriched cores can yield anomalously old ages if zonation is not accounted for (Reiners et al., 2004). Similarly, grains with U-Th-enriched rims will yield anomalously young ages. However, the date dispersion triggered by U-Th zonation is commonly 10%–15% and perhaps up to 30%–40% only in grains with extreme zonation (Ault & Flowers, 2012; Brown et al., 2013; Fitzgerald et al., 2006). In this study, most anomalous He ages are older than 160 Ma and significantly deviate from the central ages. Often the determined age was older than the intrusive age of the host magmatic rock, except for four ZHe ages (i.e., TSL6-7, WXL6-4, DYS1-3, and DYS1-6). U-Th zonation is less likely to result in these extremely old He ages but may produce slightly dispersed young He ages such as in samples WXL5-3, BS1-3, and BS2-3. There are previous reports of zircons from this region with U-Th-enriched rims resulting from intensive hydrothermal alteration (Jiang et al., 2020; Wu et al., 2018).

Undetected U-Th-rich minerals (e.g., xenotime and monazite) or He-bearing fluid inclusions are the most likely reason for the anomalously old He ages. These tiny minerals or fluid inclusions can occur via microscopic exsolution, despite attempts to pick inclusion-free zircon/apatite grains. The investigated granitoid plutons are mostly highly evolved and U-Th-rich minerals (e.g., coffinite, thorite, and uranium oxides) are widely intergrown with zircons as indicated by many studies (Jiang et al., 2020; H. Li et al., 2018; Wu et al., 2018). It is, therefore, the most likely that the old He ages resulted from the undetected presence of inclusions enriched in parent isotopes.

Other mechanisms including zircon/apatite chemical composition, complicated thermal history, and broken crystal, may also affect He age dispersion (Barbarand et al., 2003; Brown et al., 2013; Crowley et al., 1991; Willett et al., 2017). However, there is no enough evidence for systematic correlation between any of these parameters and grains that yielded anomalously old ages analyzed in this work.

5.2. Post-Triassic Thermal History of the Intracontinental CB

Samples of Tongshanling, Baoshan, Qitianling, and Wangxianling plutons were collected from transects at different elevations. None of the plutons display a positive correlation between ZHe ages and elevations, with all displaying either no (Figure 8a) or negative correlations (Figures 8b–8d). Normally, if samples are collected from the isotherm-unperturbed area by elevation, ZHe ages will positively correlate with elevations (Fitzgerald & Malusà, 2019). However, the patterns observed here are uncommon probably due to a changed paleosurface or structural deformation (Fitzgerald & Malusà, 2019). The shape of geothermal gradient is of fundamental importance to slopes of age–elevation profile (i.e., apparent or actual exhumation rate) and notably associated with shapes of paleo-topography, thermal events, and structural deformation. Although sampling strategic efforts have been made to minimize misfits between age-elevation slopes and actual exhumation history, the thermal history of Baoshan pluton is indicative of a rapid emplacement at shallow depth that undoubtedly perturbed the thermal structure of paleo-geothermal gradient. In this case, a negative slope of age-elevation profile may be obtained (Figure 8b). In addition, the Jurassic–Cretaceous faults are extensively developed in the intracontinental CB including thrust faults (e.g., Chenzhou–Linwu Fault) and detachment faults (e.g., Mufushan, Hengshan, Wugongshan, and Lushan regions) (Ji et al., 2018; J. Li et al., 2014). Faulting deformation is widespread in the other three plutons (i.e., Tongshanling, Qitianling, and Wangxianling plutons) and the faulting favors a diversified

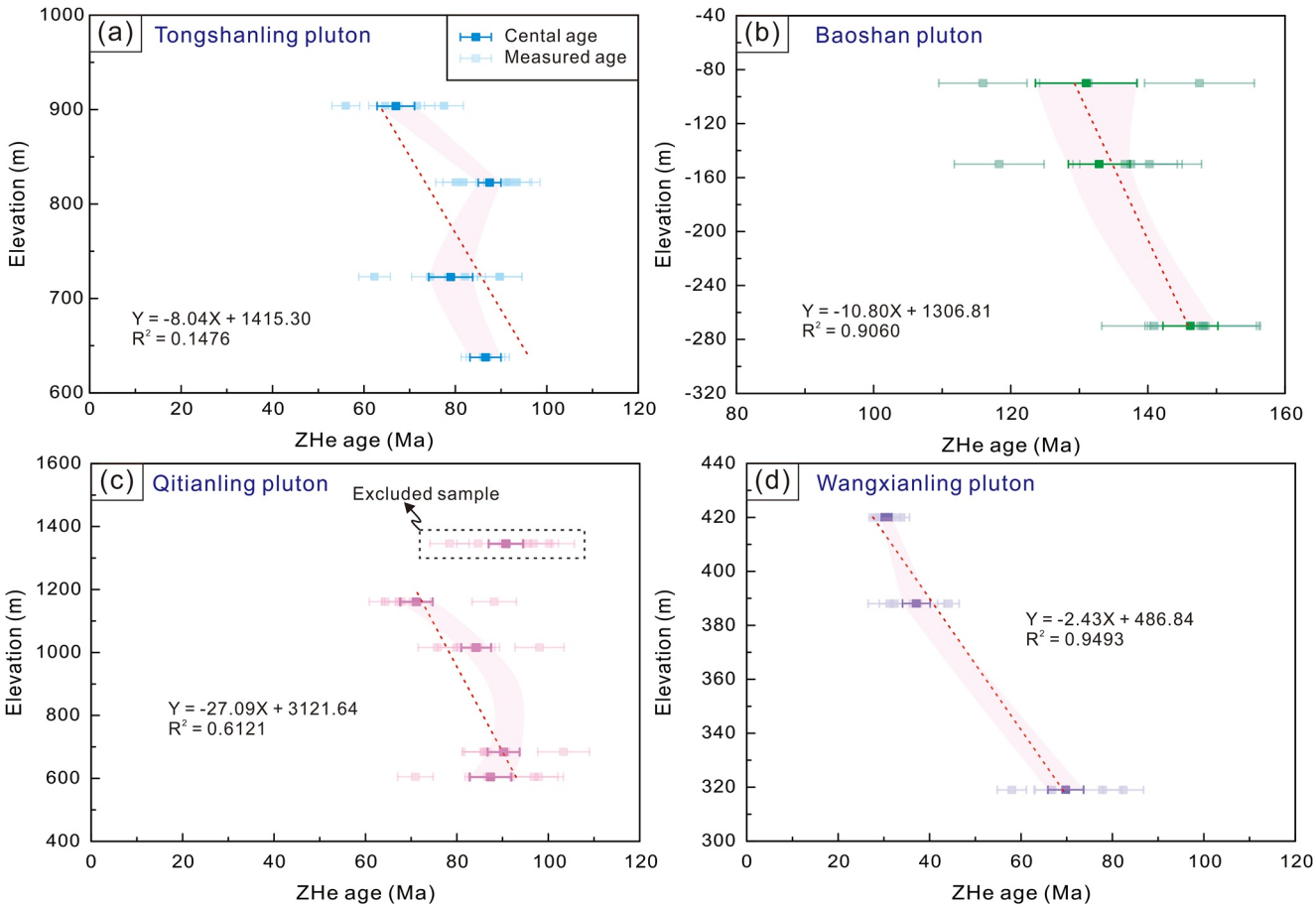

Figure 8. ZHe date versus elevation profiles of (a) Tongshanling pluton; (b) Baoshan pluton; (c) Qitianling pluton (Sample QTL-6 was excluded as it is away from sampling transect, see Figure 2); and (d) Wangxianling pluton.

exhumation of samples (Jolivet et al., 2010; Li, Dong, et al., 2016; Wu et al., 2021). For example, samples from Qitianling pluton were collected from two walls of the Chenzhou–Linwu Fault and the reverse faulting favored that the footwall was later exhumed than the deep hanging wall (Figure 2). This is likely the reason why sample QTL-5 has the highest elevation but youngest ZHe age in contrast to other samples. Furthermore, the three plutons occur as magmatic domes with high relief, suggesting that a significant change of paleo-relief (Figure 2). Relief changing is another potential cause of the negative slope of age-elevation profiles (Fitzgerald & Malusà, 2019). In summary, we suggest that ZHe age-elevation profiles are not applicable when estimating exhumation rates for these granitoids.

The two modeling approaches (HeFTy and QTQt) yield similar multi-stage thermal history models for each pluton. However, due to different algorithms of the two programs, HeFTy fails to generate enough acceptable models as the amount of input data increases, while QTQt can generate more detailed and tightly constrained thermal history for a large data set (Vermeesch & Tian, 2014). Given that multiple data constraints were used in inverse modeling, the QTQt modeling results were further utilized to estimate exhumation rates in this work. Typically, a cooling history of intrusive rocks begins with an early stage of fast cooling to the subsurface ambient temperature of host wall rocks (i.e., magma crystallization stage), followed by a later stage of exhumation cooling as the intrusion is slowly exhumed to the earth surface. Magma crystallization stages of the investigated plutons can be constrained by the gap between zircon and molybdenite/muscovite isotopic ages since the granitoid solidus is commonly higher than 600°C (Donaldson et al., 2003; Jacob & Moyen, 2021). Accordingly, long-term exhumation stages and cooling temperature spans of the eight granitoid plutons can be obtained and are summarized in Table 3. By assuming paleo-geothermal gradient at 25 ± 5°C/km, long-term exhumation rates vary from 0.167 to 0.250 km/Myr for Tongshanling pluton, 0.013–0.019 km/Myr for Weijia pluton, 0.111–0.167 km/Myr for Jiuyishan pluton,

Table 3
Calculated Parameters and Results of Long-Term Exhumation Rates

Granitoids	Timing of cooling phase (Ma)		Multi-phase cooling rates (°C/Myr)		Calculated long-term exhumation rates (km/Myr)
	Stage 1	Stage 2	Stage 1	Stage 2	Inverse modeling method
	Stage 3	Stage 4	Stage 3	Stage 4	
	Stage 5		Stage 5		
Tongshanling	161–100	100–97	5.6	37	0.167–0.250
	97–65	65–61	0.63	7.5	
Weijia	158–0		0.38		0.013–0.019
Jiuyishan	150–142	142–0	56	0.35	0.111–0.167
Dayishan	149–60	60–0	2.1	2.3	0.074–0.111
Baoshan	148–66	66–63	0.24	10	0.020–0.029
Qitianling	157–110	110–100	3.6	12	0.090–0.135
	100–41	41–35	0.17	5	
Wangxianling	213–133	133–82	0.25	4.3	0.059–0.089
	82–59	59–56	0	40	
	56–0		0.36		
Qianlishan	146–125	125–100	10	0.8	0.211–0.317
	100–86		10		

Note. Long-term exhumation rate = $\Delta T/(\Delta t$ *G), where ΔT and Δt are temperature and timing variations of total exhumation, respectively, and G is paleo-geothermal gradient.

0.074–0.111 km/Myr for Dayishan pluton, 0.020–0.029 km/Myr for Baoshan pluton, 0.090–0.135 km/Myr for Qitianling pluton, 0.059–0.089 km/Myr for Wangxianling pluton, and 0.211–0.317 km/Myr for Qianlishan pluton, respectively (Table 3). However, the modeling results of Weijia, Jiuyishan, Dayishan, and Wangxianling plutons lack AHe age constraints and show cooling events ended until present day in contrast to other plutons with AHe age constraints (e.g., Tongshanling and Qitianling plutons). Therefore, the four granitoids probably have much higher factual exhumation rates than those given by the modeling results.

The cooling timing and exhumation history of the studied plutons have important implications for thermal evolution of the intracontinental CB since the Triassic. Baoshan and Weijia plutons generate obviously older ZHe ages than other granitoid plutons, consistent with their hypabyssal origins (Table 1). In comparison, the other plutons mostly have Late Cretaceous ZHe ages with an exception of Jiuyishan pluton (ZHe age = 115.6 Ma). A summary of ZHe/AHe age and sampling elevation data shows that two remarkable exhumation events occurred in the intracontinental CB and promoted high elevations of these samples during the Late Cretaceous to Paleogene, with peaks at 100–80 and 50–20 Ma, respectively (Figure 9a). The earlier ZHe age of Jiuyishan pluton indicates that its exhumation predated other plutons in the intracontinental CB. The following lines of evidence support that Jiuyishan pluton was likely a thermal uplifting center in the intracontinental CB: (a) low-velocity anomalies were identified in the middle crust and upper mantle beneath the Jiuyishan region, and the external heat induced by asthenospheric mantle upwelling is considered to drive this lithospheric structural modification (He et al., 2021); (b) the presence of high temperature magmatic rocks within the Jiuyishan region (e.g., high $\delta^{18}O$ fayalite granite and tholeiitic basalt, Jiang et al., 2009; Huang et al., 2011); (c) Cretaceous basins are widespread around the Jiuyishan region (Figure 2); and (d) the high relief and ~50 km scale magmatic dome structure of the Jiuyishan region (Figures 2 and 5g). Although the intracontinental CB probably experienced widespread exhumation in the Cretaceous, a rough longitude gradient of exhumation is evident with a decrease in the onset age of stage 1 exhumation moving eastward (Table 3; Figure 9d). This spatiotemporal variation further indicates that the western side of the Chenzhou–Linwu Fault may have been exhumed prior to the Early Cretaceous. Moreover, long-term exhumation rates of these plutons roughly increase from the west to the east, suggesting that the western range seems to be affected by weaker exhumation (Figure 9d).

The inverse modeling results also indicate that the intracontinental CB experienced long-lived multi-phase rapid exhumation (>10°C/Ma) commencing from the Jurassic, such as the Late Jurassic (e.g., 150–142 Ma of Jiuyishan pluton), Early Cretaceous (e.g., 110–100 Ma of Qitainling pluton), Late Cretaceous (e.g., 100–97 Ma of Tongshanling pluton and 100–86 Ma of Qianlishan pluton), and the Paleogene (e.g., 66–63 Ma of Baoshan pluton, and 59–56 Ma of Wangxianling pluton), although each pluton varies in the quantity and timing of exhumation phases (Figures 5 and 6). Based on integrated and average t-T paths of the eight granitoids, three common notable exhumation stages are identified in the intracontinental CB: (a) 150–110 Ma (peaking at 143–110 Ma), (b) 110–85 Ma (peaking at 110–97 Ma), and (c) 66–38 Ma (peaking at 64–40 Ma), with a thermal lull of 85–66 Ma (Figure 10). Cooling rates of the three stage exhumations are 4.0°C/Ma, 5.3°C/Ma, and 1.1°C/Ma, respectively, suggesting that these plutons were rapidly exhumed (~7.2 km, calculated by using temperature range of ~240–60°C and paleo-geothermal gradient at 25°C/km) in the Cretaceous (143–85 Ma; Figure 10). This in good agreement with intensive Cretaceous ZHe ages in the intracontinental CB (Figure 9a) and widespread detrital zircons of Cretaceous and Jurassic ages in the Hengyang Basin (Figure 2; Y. Yan et al., 2011). In contrast, the 85–66 Ma slow cooling demonstrates a weakened tectonism in the intracontinental CB during the Latest Cretaceous, as recoded by the reducing amount of low-temperature chronological ages in the intracontinental CB (Figure 9a) and a sedimentary disconformity of 70–66 Ma in the Chaling Basin (Figure 2; Xu et al., 2021).

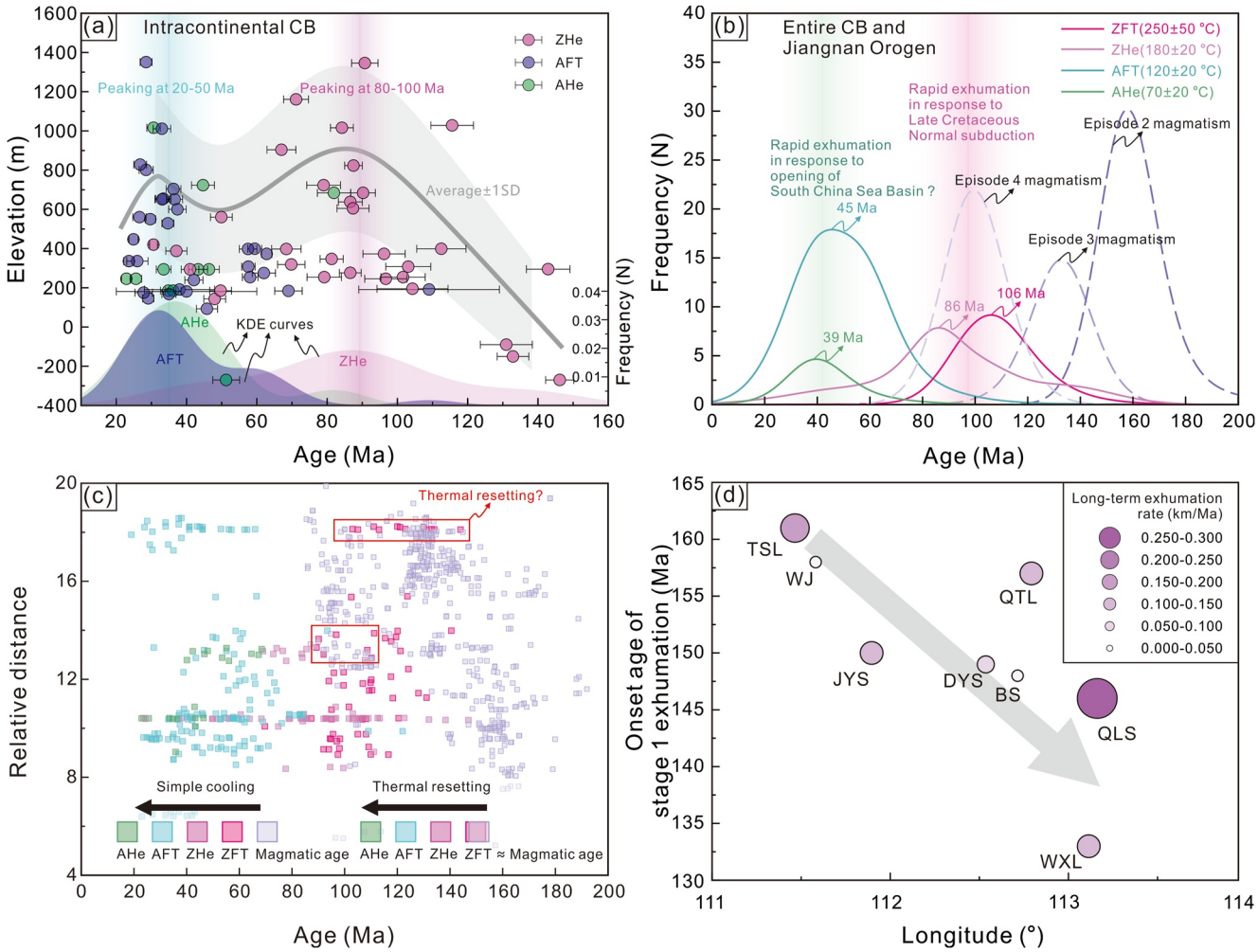

Figure 9. (a) Plot of low-temperature thermochronological date versus sampling elevation of samples from the intracontinental Cathaysia Block, with in the range of 24.5°–26.5°N and 111.0°–114.0°E (Table S4; gray error margin is calculated based on every 10 Myr from 20 Ma). (b) Kernel density estimation (KDE) curves of magmatic episodes, zircon fission track, ZHe, apatite fission track, and AHe dates of the entire Cathaysia Block and Jiangnan Orogen. (c) Plot of age versus relative distance to datum point (105°E, 20°N) for evaluating the influence of thermal resetting associated with magma emplacement. (d) Plot of onset age of stage 1 exhumation versus sample longitude, with color mapping for long-term exhumation rates.

The onset timing of exhumation phases of the studied plutons (Figures 5 and 6) mostly postdates the Late Jurassic. The inverse modeling curves of the Triassic Wangxianling pluton seem to be stabilized at 390 ± 10°C isotherm throughout the Jurassic (Figure 6g). In addition, Y. Yan et al. (2011) suggested that sedimentary provenances of the Upper Triassic–Middle Jurassic and Lower Cretaceous sandstones from the Hengyang Basin are contrasting with the former dominated by pre-Mesozoic-rock source and the latter dominated by Triassic magmatic rocks. Previous studies also suggested that no Early–Middle Jurassic fast cooling occurred in the sub-epicontinental and epicontinental CB, with only local reheating events induced by magma emplacement (Tao et al., 2017, 2019). These lines of evidence imply that the intracontinental CB was not significantly exhumed at least before the Late Jurassic. The remarkable exhumation of granitic plutons in the intracontinental CB was structurally induced by a series of Cretaceous extensional tectonism (e.g., normal faulting, detachment faulting, and fault block tilting), as well documented in the adjacent Hengshan, Mufushan, and Yuechengling plutons (Feng et al., 2022; Ji et al., 2018; Li, Shi, et al., 2016).

5.3. Implications for Geodynamics Driving the CB Polyphase Exhumation

Climate-induced erosion tends to sculpt near-surface landform, whereas the significant exhumation of Mesozoic intrusive rocks (~3–10 km exhumation) in the CB was likely a tectonic response to deep geological processes.

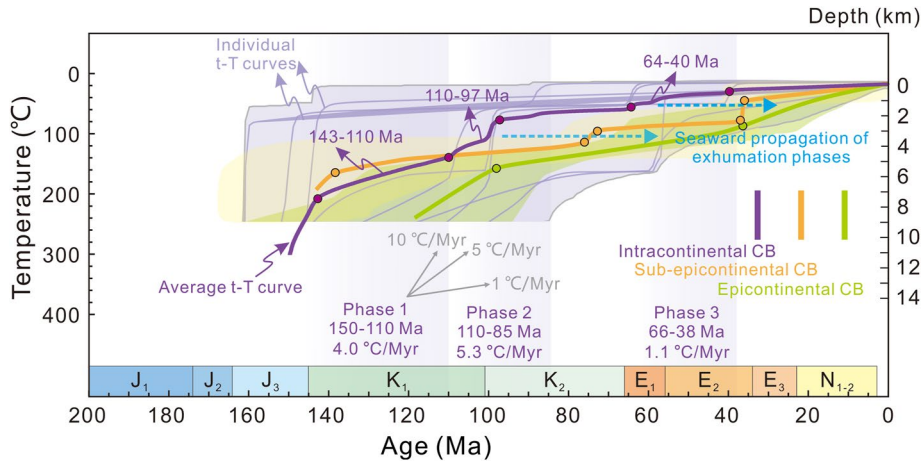

Figure 10. A summary of inverse modellings of the investigated granitoids indicating a three-stage exhumation in the intracontinental Cathaysia Block.

Therefore, a clarity of exhumation history of the entire CB is crucial to unravel the underlying geodynamic processes. However, exhumation history of the CB remains elusive due to a handful of low-temperature thermochronological studies. Until recently, low-temperature thermochronological studies just sprang up and revealed a large variation of (U-Th)/He and fission track ages in the CB (e.g., Su et al., 2017; Sun et al., 2021; Tao et al., 2017, 2019; Y. J. Wang et al., 2020a). Previously published ZHe and AHe ages are locally reported and range in the intervals of 152–24 Ma (peaking at 86 Ma, $n = 82$) and 69–23 Ma (peaking at 39 Ma, $n = 30$), respectively (Table S4 in Supporting Information S1). In contrast, ZFT and AFT ages have been extensively presented with onset time spans of 144–70 Ma (peaking at 106 Ma, $n = 71$) and 93–24 Ma (peaking at 45 Ma, $n = 167$), respectively (Figure 11, Table S4 in Supporting Information S1).

The varied thermochronological data complicated interpretations to exhumation history of the CB, in particularly since the Early Cretaceous. In the intracontinental CB, for example, Su et al. (2017) investigated Mesozoic rocks in both sides of the Chenzhou–Linwu Fault (Figure 1a) and suggested that exhumation occurred in two episodes at 45–35 and 36–23 Ma, respectively. Sun et al. (2021) indicated a two-stage exhumation of the Changjiang uranium ore field (sub-epicontinental CB) at ~80–60 and ~40–0 Ma. In contrast, Ding et al. (2019) pointed out one exhumation event from ~150 to 110 Ma and another one between ~100 and 80 Ma that took place in the southeastern epicontinental CB. Tao et al. (2017) indicated ~140–70 and ~53–36 Ma exhumation of the southern epicontinental CB. Based on regional AFT analyses, Y. A. Wang et al. (2020a) identified two major exhumation events in the CB occurring in the Cretaceous (~125–80 Ma) and Late Cretaceous–Paleogene (~80–25 Ma). The diversified interpretations of the CB exhumation history result in part from a complicated Mesozoic to Cenozoic tectonism. On the other hand, given that inverse modeling results of HeFTy program depend on the amount of input data and t-T constraints, it is difficult to reproduce consistent thermal models as inverse modeling strategies vary in previous studies (Vermeesch & Tian, 2014).

In comparison, our mutually validated thermochronological modeling results register a more constrained three-phase exhumation history of the intracontinental CB, which commenced in the Late Jurassic–Early Cretaceous, accelerated in the Late Cretaceous, and dissipated over the widespread Paleogene, regardless of some localized differences (Figure 10). The inverse modeling results attest the previous models that the intracontinental CB experienced multiple exhumation phases since the Triassic (Chu et al., 2019; J. Li et al., 2014), although the onset timing is variable. Nonetheless, a rapid post-Paleogene (<23 Ma) exhumation is not observed in most samples, suggesting that post-Paleogene tectonism was more limited and weaker within the intracontinental CB than previously suggested (Su et al., 2017; Sun et al., 2021; Tao et al., 2017, 2019).

To avoid being biased by local data, thermochronological mapping is utilized to further constrain exhumation history of the entire CB. Due to the extensive magmatic emplacement across the CB, a potential thermal resetting for regional thermal field requires an evaluation (B. Wang et al., 2014). As shown in Figure 9c, the majority of magmatic ages is older than the compiled low-temperature thermochronological data, except for some ZFT ages,

10.1029/2022TC007662

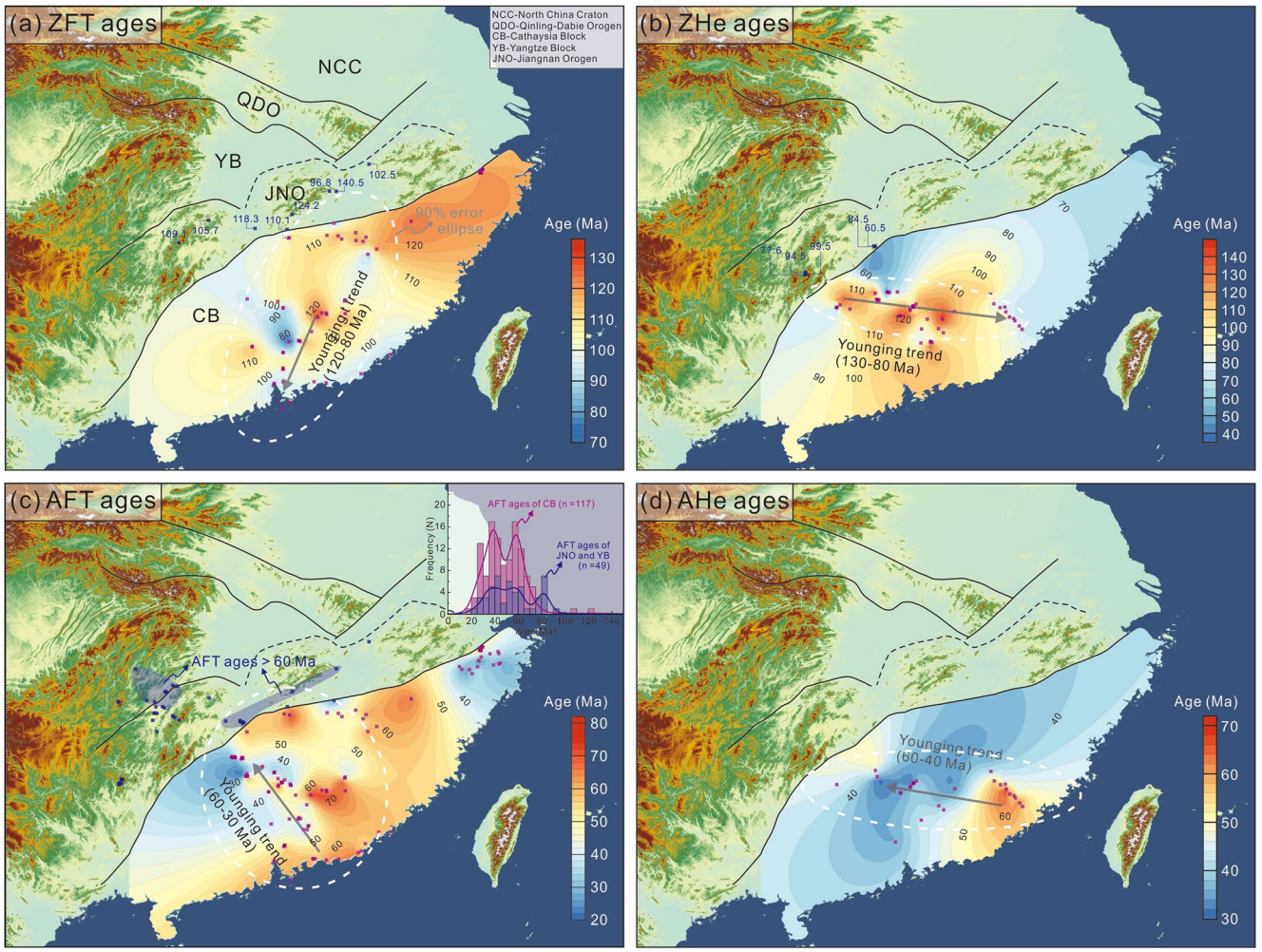

Figure 11. Contour maps of (a) post-Triassic zircon fission track dates; (b) post-Triassic ZHe dates; (c) post-Triassic apatite fission track dates with frequency diagram showing AFT dates in different tectonic belts; and (d) post-Triassic AHe dates in the Cathaysia Block (Data source: Chu et al., 2020; Ding et al., 2019; Li, Shi, et al., 2016; Li & Zou, 2017; Qiu et al., 2019; Su et al., 2017; Sun et al., 2021; Tao et al., 2017, 2019; Tang et al., 2014; Yi et al., 2009; Wang et al., 2015, 2018, 2020a, 2020b).

elucidating that the thermal resetting associated with magma emplacement is negligible. A synthesis of ZHe/ZFT dates (Figures 11a and 11b) shows that the intracontinental CB was exhumated to the ZPRZ (~5–10 km under the surface) prior to the epicontinental CB in the Early Cretaceous (~130–110 Ma). In contrast, regional AFT/AHe data demonstrates a sketchy aging trend (from 30 Ma to 60 Ma) toward the southeastern CB (Figures 11c and 11d). This indicates that exhumation in the intracontinental CB weakened progressively and the epicontinental CB underwent much significant exhumation of ~1–5 km during the Latest Cretaceous–Paleogene (~70–30 Ma).

The thermochronological patterns argue against Alpine type continental collision, continental rifting, and normal oceanic subduction models which facilitate earlier fast exhumation of epicontinental CB than intracontinental CB (Gilder et al., 1996; Hsü et al., 1988; Y. J. Wang et al., 2008). In comparison, a flat-slab subduction model is more plausible, in which the Paleo-Pacific Plate initiated flat-slab subduction prior to the Late Jurassic with slab break-off occurring in the Late Jurassic. The broken-off slab caused asthenosphere mantle upwelling and progressive slab roll-back processes in the Cretaceous. The foundering of broken-off slab may trigger for intensive magmatism and preceding exhumation in intracontinental CB. The prolonged Cretaceous exhumation episode and seaward exhumation propagation patterns were most likely induced by mantle-upwelling-driven crustal thinning and tectonic uplift (e.g., magmatic doming, normal fault slip, and detachment faulting) during the slab retreating processes (Li, Shi, et al., 2016). In addition, the exhumation continuity (from the Early to Late Cretaceous) of the intracontinental CB is consistent with suggested duration of subduction of the Paleo-Pacific

Plate (at least from 145 to 85 Ma), implying that the oceanic subduction was likely the first-order driver for regional exhumation (Figure 10, J. Li et al., 2014). The progressive southeastward propagation of fast exhumation phase implies that the subduction slab reached the intracontinental CB at least earlier than 130 Ma and gradually retreated to the epicontinental CB by 90–80 Ma (Figures 11a–11d). We also synthesized previous thermal modeling results of the sub-epicontinental and epicontinental CB (Figure 10; X. Shi et al., 2022; Tao et al., 2019). Interestingly, integrated thermal modeling curves show stepwise lagged exhumation phase from the intracontinental to the seawards epicontinental CB, in particularly from the 120 Ma, in good agreement with inferred slab retreating processes (Figure 10). The slab retreating processes are further supported by consistent peaks of regional ZFT/ZHe ages with episodes 3 and 4 arc magmatism ages of the CB (Figure 9b). In addition, low-temperature thermochronological data from the Jiangnan Orogen generated similar ages to those of the CB. Nevertheless, thermochronological data from the Yangtze Block display much older ages (e.g., AFT ages peaking at ~80 Ma, Figure 11c). The contrasting patterns of thermochronological data from the Yangtze Block indicate that the advance of subduction slab was farthest restricted to the Jiangnan Orogen as supported by the lack of Jurassic granites in the west of the Jiangnan Orogen (Figure 1a). Therefore, thermochronological data from the CB indicate that the oceanic slab may reach confined to the west of the Yangtze Block and progressively retreated to the epicontinental CB in 90–80 Ma.

AFT/AHe ages of the entire CB are clustered between ~60 and 20 Ma and peak at ~40 ± 10 Ma (Figures 9a and 9b), which show a younging trend from the SE epicontinental to intracontinental CB (Figures 11c and 11d). In contrast, AFT/AHe data obtained from the Yangtze Block (e.g., eastern Sichuan Basin, H. Shi et al., 2016) differ those of CB by a widespread record of Neogene thermal events related to upward and eastward growth of the Tibetan Plateau. Such contrasting AFT/AHe patterns suggested that the Paleogene increase in exhumation rates seem to be correlated with a regional tectonism. In the intracontinental CB and Jiangnan Orogen, numerous faults and folds have been recognized in the Upper Cretaceous–Paleogene strata of the Jianghan and Yuanma Basins, which are unconformably overlain by the Neogene strata (J. H. Li et al., 2012). Thus, the Paleogene exhumation of the CB was more likely as a far-field tectonic response to the opening of the South China Sea Basin (the Paleogene ~ N–S-directed spreading directions; Camanni & Ye, 2022; Gan et al., 2022). This inference is consistent with widespread E− or ESE-striking normal faults in the CB (kinematically indicative of the Latest Cretaceous–Early Paleogene ~ N–S extension; J. Li et al., 2014; J. H. Li et al., 2012). However, due to the feedback between erosion and tectonic uplift, it is difficult to clearly differentiate a tectonic cause from a climate-induced cause of fast exhumation during near-surface processes (Willett et al., 2021). Therefore, climate-driven erosion for the intracontinental CB cannot be totally excluded.

5.4. Multi-Perspective Constraints on the Oceanic Plate Subduction Processes

As documented by the compiled data set, the earliest low-temperature thermochronological date related to the Mesozoic tectonism in the CB is 152 Ma (Table S4 in Supporting Information S1). Since utilization of low-temperature thermochronology is primarily restricted to shallow geological processes (<300°C), the early or deep geological processes associated with the Paleo-Pacific Plate subduction beneath the SCB require constraints from other geologic perspectives.

Despite hot debates on the onset timing of Paleo-Pacific Plate subduction (syn-Triassic vs. post-Triassic), the Jurassic to Cretaceous magmatism and tectonism have been proven as by-products of the oceanic subduction (Cao et al., 2021; J. Li et al., 2014; Li & Li, 2007; Zhou et al., 2006). The Jurassic magmatism is characterized by voluminous granitoids and sporadic mantle-derived rocks (Cao et al., 2021; Zhou et al., 2006). According to the spatiotemporal pattern of Jurassic magmatism (Figure 7b), the earliest Jurassic magmatism took place in the sub-epicontinental CB and arc magmatism was handful in the epicontinental CB (Cao et al., 2021; Zhou & Li, 2000). The location and petrogenesis of the Jurassic arc magmatism favor a low-angle subduction model. This is because of a slow increase of heat and pressure during the low-angle subduction that prevents the slab from large-scale partial melting and dehydration, as a result of which a long subduction distance is required for generating magmatism. Structurally, Jurassic NE-striking thrusts and fault-related folds are well developed across the SCB. In the Yangtze Block, thin- and thick-skinned thrust sheets have accommodated ~160 km of shortening by in- and out-of-sequence thrusting above a series of décollements (Figure 12; D. P. Yan et al., 2009; J. Li et al., 2014). In the CB, regional-scale refolded folds are well developed by superimposed Jurassic NE-trending and Triassic ~ E–W-trending anticlinoria. The fold interference pattern exhibits as the classic dome-and-basin

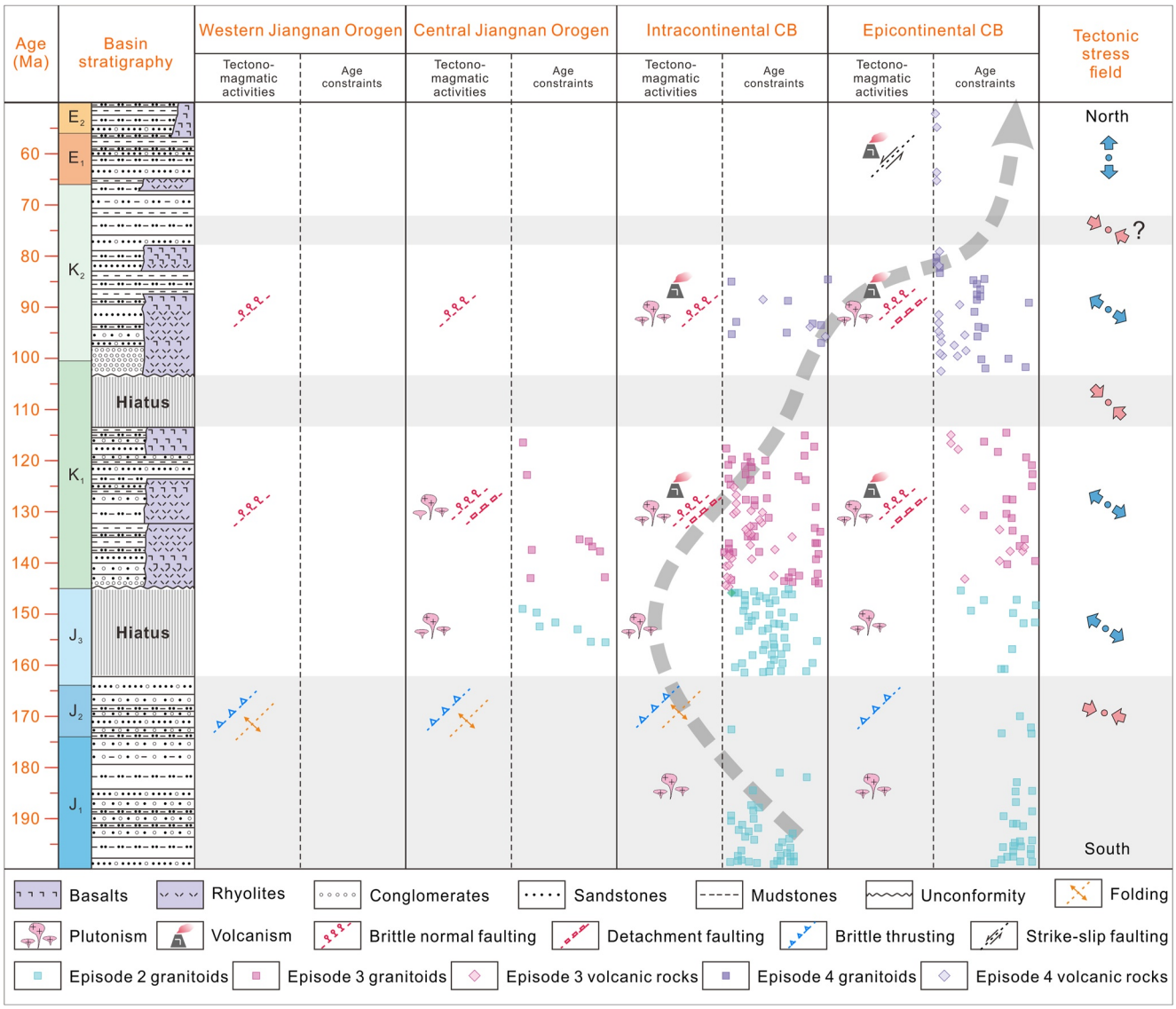

Figure 12. Spatiotemporal plot of the compiled geochronological and tectonic data from the Cathaysia Block and Jiangnan Orogen. The gray arrow indicates the evolution of tectono-magmatic activities.

structure (Type 1) with wavelengths of tens of kilometers (W. Shi et al., 2015). The youngest strata involved in thrusting and faulting is the Middle Jurassic, indicating that SCB was under a contractional regime during the Early–Middle Jurassic, and the contractional deformation peaked immediately after the deposition of the Middle Jurassic strata as marked by the Late Jurassic hiatus (Figure 12). The leading model for driving intraplate contractional deformation is flat-slab subduction, whereby stress coupling of a downgoing oceanic plate to the upper plate transmitted stresses inlandward, producing a broad intraplate contractional regime characterized by extensive fold-and-thrust belt and décollement formation but with less arc magmatism (English et al., 2003; English & Johnston, 2004). This is well documented in the broad Rocky Mountain fold-and-thrust belt that was formed by the flat-slab subduction of the Kula–Farallon Plate (Murphy et al., 2003), and is reconciled with the geological observations in the CB during the Early–Middle Jurassic. With the ongoing low-angle subduction processes, slab reached the intracontinental CB and broke off due to the gravitational instability in the Late Jurassic (~160–150 Ma). The foundering of broke-off slab caused an upwelling of asthenosphere and consequent lithospheric extension, whereby the intensive magmatism occurred in the intracontinental CB. This interpretation is consistent with thermal histories of some pre-Cretaceous rocks in the epicontinental CB that indicate a potential

Late Jurassic thermal resetting for their low-temperature thermochronological system, which were related to the granitoid magmatism (Tao et al., 2017, 2019).

Most Cretaceous magmatic rocks of the CB are volcanic arc rocks (e.g., rhyolite, dacites, andesites, and basalts, J. Li et al., 2014; Cao et al., 2021). Furthermore, the notable NE-striking extensional basins and magmatic belts indicate a coeval NW–SE crustal extension in the CB, related to an ongoing lithospheric extension caused by the Late Jurassic foundering of broke-off oceanic slab. In contrast to the Jurassic magmatism, the Cretaceous magmatism was shifted from the intracontinental to the sub-epicontinental and epicontinental of CB in the Early and Late Cretaceous, respectively (Figures 7c–7d, Cao et al., 2021). Furthermore, Cretaceous mafic magmatism is more intensive than that of the Jurassic, and high-angle oceanic subduction favors extensive dehydration of the slab and the addition of slab-derived fluid/melt contributes greatly to the partial melting of mantle (Meng et al., 2012). This is further evidenced by the generation of voluminous volcanic rocks in the CB since the Early Cretaceous (Figure 12). This spatiotemporal pattern of Cretaceous magmatism decodes that the Jurassic low-angle subduction had been converted into a normal subduction and retreated as a consequence of the tugging of foundered slab. Numerous NE-striking brittle normal faults, low-angle detachments, and ductile shear zones were formed in the entire CB by the retreating of subducted oceanic slab (Figure 12).

The Cretaceous rapid exhumation history of the CB was also consistent with the interplay of tectonism and topography. Based on the thermochronological synthesis, we found that AHe and AFT ages of the CB roughly show an aging propagation from the intracontinental to the epicontinental CB, without thermal resetting by magma emplacement, suggesting that the epicontinental CB was foremost exhumated to the surface and formed a paleo high-relief margin. Slab roll-back has been well documented to cause notable surface uplift and exhumation of the overriding plate, such as proposed for the Puna Plateau-Sierra Pampeanas (Gvirtzman & Amos, 1999; Kay & Coira, 2009). Sedimentary study elucidates different sedimentary provenances of the Lower and Upper Cretaceous sandstones of the CB (Triassic and Jurassic–Cretaceous magmatic rock source, respectively), consistent with a significant exhumation of the Jurassic to Lower Cretaceous magmatic rocks during the Late Cretaceous to Paleogene (Y. Yan et al., 2011). This exhumation seems to initiate from the Late Cretaceous as indicated by different sediment provenances and widespread unconformity of Upper and Lower Cretaceous sedimentary rocks (J. Li et al., 2014). In addition, the paleo-river-network has been recognized to flow westwards from the epicontinental CB and debouch in inland lakes (Shu et al., 2009). These lines of evidence indicate an existence of mountain belt in the epicontinental CB during the Late Cretaceous to the Early Paleogene. In the high Rocky Mountains, slab roll-back of the Farallon Plate was considered as the main driver for seaward migration of surface elevation uplift, notable exhumation, and magmatism, in good agreement with the case of the Cathaysia Block (Fan & Carrapa, 2014).

In summary, the multi-perspective geological evidences, together with spatiotemporal patterns of the Mesozoic low-temperature thermochronological data, illustrate a trilogy of subduction processes of the Paleo-Pacific Plate: (a) in the Early Jurassic, the subduction of Paleo-Pacific Plate was at a low angle and the slab reached the intracontinental SCB probably during the Middle Jurassic (Figure 13a), with slab break-off occurring in the Late Jurassic (Figure 13b); (b) in the Early Cretaceous, the oceanic subduction gradually increased the subduction angle as pulled by the foundering slab (Figure 13c); and (c) in the Late Cretaceous, the slab retreated to the epicontinental CB, changed into a normal subduction, and generated voluminous arc plutonism and volcanism (Figure 13d). In this scenario, the Cretaceous retreating subduction processes of the Paleo-Pacific Plate were responsible for notable exhumation of the CB, with minor exhumation probably related to the Paleogene opening of the South China Sea Basin.

6. Conclusions

1. ZHe/AHe data and inverse modeling results suggest the intracontinental CB experienced three-stage rapid exhumation from the Late Jurassic to Paleogene with variable onset timing and the far intracontinental CB (the west of the Chenzhou–Linwu Fault) was exhumed earlier than the Early Cretaceous.
2. Regional contour maps of low-temperature thermochronological data favor advancing and retreating subduction processes of the Paleo-Pacific Plate and opening of the South China Sea Basin as major geodynamic triggers for Cretaceous and Paleogene exhumation of the CB, respectively.
3. Cretaceous rapid exhumation of the CB, especially in the Late Cretaceous, were crucial to the topographic evolution, and raised a mountain belt in the epicontinental CB.

10.1029/2022TC007662

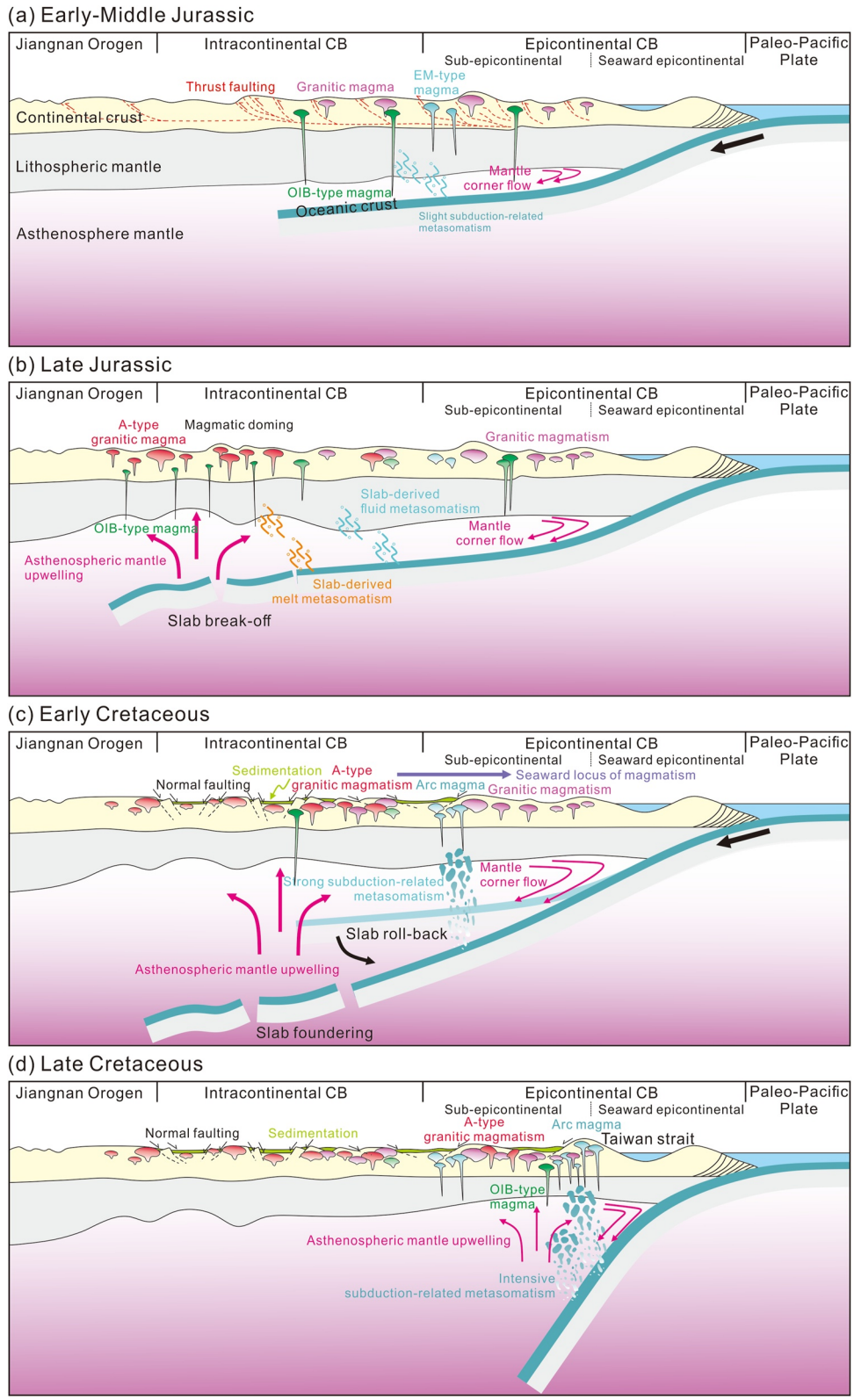

Figure 13. A cartoon illustrating the tectonic evolution of the Cathaysia Block: (a) Early–Middle Jurassic low-angle subduction; (b) Late Jurassic slab break-off; (c) Early Cretaceous progressive slab retreat with slab foundering; and (d) Late Cretaceous normal subduction.

4. Spatiotemporal variations of low-temperature thermochronological data and multiple geological observations are consistent, indicating that the Paleo-Pacific Plate developed low-angle subduction in the Early–Middle Jurassic, and that the plate underwent slab break-off and foundering in the Late Jurassic, with subduction slab gradually retreating to the epicontinental CB and being transformed to a normal sense during the Cretaceous.

Data Availability Statement

The (U-Th)/He analytical results and compiled low-temperature thermochronology data are included in the Supporting Information and hosted at Mendeley data (https://doi.org/10.17632/vpgcdwn569.3).

Acknowledgments
This work was co-financed by Natural Science Foundation of Hunan Province (2022JJ30699), National Key Research and Development Plan (2018YFC0603902), and the Fundamental Research Funds for the Central Universities of Central South University (2021zzts0252). Mr. Jinghua Wu was funded by the China Scholarship Council (202006370297) during his visiting and study at the Kyushu University, Japan, which is greatly acknowledged. Dr. Martin Danišík was supported by Australian Scientific Instruments Pty Ltd., Australian Research Council (ARC) Discovery funding scheme (DP160102427) and a Curtin Research Fellowship (CRF170135). We would like to thank Dr. Huashan Sun for helpful discussion. We are grateful to Prof. Noreen J. Evans for her constructive comments and great help to improve this paper. The supplementary data of this paper can be freely accessed on the Mendeley Data at https://data.mendeley.com/drafts/vpgcdwn569 (https://doi.org/10.17632/vpgcdwn569.3).

References

Ault, A. K., & Flowers, R. M. (2012). Is apatite U–Th zonation information necessary for accurate interpretation of apatite (U–Th)/He thermochronometry data? *Geochimica et Cosmochimica Acta*, *79*, 60–78. https://doi.org/10.1016/j.gca.2011.11.037

Barbarand, J., Carter, A., Wood, I., & Hurford, T. (2003). Compositional and structural control of fission-track annealing in apatite. *Chemical Geology*, *198*(1–2), 107–137. https://doi.org/10.1016/S0009-2541(02)00424-2

Brown, R. W., Beucher, R., Roper, S., Persano, C., Stuart, F., & Fitzgerald, P. (2013). Natural age dispersion arising from the analysis of broken crystals. Part I: Theoretical basis and implications for the apatite (U–Th)/He thermochronometer. *Geochimica et Cosmochimica Acta*, *122*, 478–497. https://doi.org/10.1016/j.gca.2013.05.041

Camanni, G., & Ye, Q. (2022). The significance of fault reactivation on the Wilson cycle undergone by the northern South China Sea area in the last 60 Myr. *Earth-Science Reviews*, *225*, 103893. https://doi.org/10.1016/j.earscirev.2021.103893

Cao, X., Flament, N., Li, S., & Müller, R. D. (2021). Spatio-temporal evolution and dynamic origin of Jurassic-Cretaceous magmatism in the South China Block. *Earth-Science Reviews*, *217*, 103605. https://doi.org/10.1016/j.earscirev.2021.103605

Cawood, P. A., Zhao, G., Yao, J., Wang, W., Xu, Y., & Wang, Y. (2018). Reconstructing south China in Phanerozoic and Precambrian supercontinents. *Earth-Science Reviews*, *186*, 173–194. https://doi.org/10.1016/j.earscirev.2017.06.001

Chen, J., Qingfei, W., Qiao, L., Liu, X., & Zhang, Q. (2020). Cretaceous exhumation history of the southwestern South China Block: Constraints from fission-track thermochronology. *Geological Journal*, *55*(10), 6718–6731. https://doi.org/10.1002/gj.3837

Cherniak, D. J., & Watson, E. B. (2001). Pb diffusion in zircon. *Chemical Geology*, *172*(1–2), 5–24. https://doi.org/10.1016/S0009-2541(00)00233-3

Chew, D. M., & Spikings, R. A. (2015). Geochronology and thermochronology using apatite: Time and temperature, lower crust to surface. *Elements*, *11*(3), 189–194. https://doi.org/10.2113/gselements.11.3.189

Chu, Y., Faure, M., Zhenhua, X., Ji, W., & Feng, Z. (2019). Cretaceous episodic extension in the South China Block, East Asia: Evidence from the Yuechengling Massif of Central South China. *Tectonics*, *38*(10), 3675–3702. https://doi.org/10.1029/2019TC005516

Chu, Y., Lin, W., Faure, M., Allen, M. B., & Feng, Z. (2020). Cretaceous exhumation of the Triassic intracontinental Xuefengshan Belt: Delayed unroofing of an orogenic plateau across the South China Block? *Tectonophysics*, *793*, 228592. https://doi.org/10.1016/j.tecto.2020.228592

Crowley, K., Cameron, M., & Schaefer, R. (1991). Experimental studies of annealing of etched fission tracks in fluorapatite. *Geochimica et Cosmochimica Acta*, *55*(5), 1449–1465. https://doi.org/10.1016/0016-7037(91)90320-5

Danišík, M., McInnes, B. I., Kirkland, C. L., McDonald, B. J., Evans, N. J., & Becker, T. (2017). Seeing is believing: Visualization of He distribution in zircon and implications for thermal history reconstruction on single crystals. *Science Advances*, *3*(2). https://doi.org/10.1126/sciadv.1601121

Danišík, M., Štěpančíková, P., & Evans, N. J. (2012). Constraining long-term denudation and faulting history in intraplate regions by multisystem thermochronology: An example of the Sudetic Marginal Fault (Bohemian Massif, central Europe). *Tectonics*, *31*(2). https://doi.org/10.1029/2011TC003012

Ding, R., Min, K., & Zou, H. (2019). Inversion of topographic evolution using low-T thermal history: A case study from coastal mountain system in southeastern China. *Gondwana Research*, *67*, 21–32. https://doi.org/10.1016/j.gr.2018.09.009

Donaldson, C. H., Reavy, R. J., & O'Mahony, M. J. (2003). Plutonic geology. In R. A. B. T. E. of P. S. and T. (T. E. Meyers (Ed.) (pp. 491–508). Academic Press. https://doi.org/10.1016/B0-12-227410-5/00588-3

English, J., & Johnston, S. (2004). The Laramide Orogeny: What were the driving forces? *International Geology Review*, *46*(9), 833–838. https://doi.org/10.2747/0020-6814.46.9.833

English, J., Johnston, S., & Wang, K. (2003). Thermal modelling of the Laramide orogeny: Testing the flat-slab subduction hypothesis. *Earth and Planetary Science Letters*, *214*(3–4), 619–632. https://doi.org/10.1016/S0012-821X(03)00399-6

Evans, N., Byrne, J., Keegan, J., & Dotter, L. (2005). Determination of uranium and thorium in zircon, apatite, and fluorite: Application to laser (U-Th)/He thermochronology. *Journal of Analytical Chemistry*, *60*(12), 1159–1165. https://doi.org/10.1007/s10809-005-0260-1

Fan, M., & Carrapa, B. (2014). Late Cretaceous-early Eocene Laramide uplift, exhumation, and basin subsidence in Wyoming: Crustal responses to flat slab subduction. *Tectonics*, *33*(4), 509–529. https://doi.org/10.1002/2012TC003221

Faure, M., Lin, W., Chu, Y., & Lepvrier, C. (2016). Triassic *tectonics,* of the southern margin of the South China Block. *Comptes Rendus Geoscience*, *348*(1), 5–14. https://doi.org/10.1016/j.crte.2015.06.012

Feng, Z., Chu, Y., Wei, W., Lin, W., Xin, G., Wang, Y., et al. (2022). Splitting a large pluton by Cretaceous crustal extension: Evolution of the Ziyuan detachment and crustal thinning of the South China Block. *Tectonophysics*, *838*, 229481. https://doi.org/10.1016/j.tecto.2022.229481

Fitzgerald, P., & Malusà, M. (2019). Concept of the exhumed partial annealing (retention) zone and age-elevation profiles in thermochronology (pp. 165–189). https://doi.org/10.1007/978-3-319-89421-8_9

Fitzgerald, P. G., Baldwin, S. L., Webb, L. E., & O'Sullivan, P. B. (2006). Interpretation of (U–Th)/He single grain ages from slowly cooled crustal terranes: A case study from the transantarctic mountains of southern Victoria Land. *Chemical Geology*, *225*(1–2), 91–120. https://doi.org/10.1016/j.chemgeo.2005.09.001

Flowers, R., Shuster, D., Wernicke, B., & Farley, K. (2007). Radiation damage control on apatite (U-Th)/He dates from the Grand Canyon region, Colorado Plateau. *Geology*, *35*(5), 447. https://doi.org/10.1130/G23471A.1

Fu, J. M., Li, H. Q., Qu, W. J., Yang, X. J., Wei, J. Q., Liu, G. Q., & Ma, L. Y. (2007). Re-Os isotope dating of the Da'ao tungsten-tin deposit in the Jiuyi Mountains, southern Hunan Province. *Geology in China*, *4*, 651–656. (In Chinese with English abstract).

Gallagher, K. (2012). Transdimensional inverse thermal history modelling for quantitative thermochronology. *Journal of Geophysical Research*, *117*(B2). https://doi.org/10.1029/2011JB008825

Gan, H., Wang, X., Wang, B., & Wang, G. (2022). Cenozoic thermal-rheological evolution of the coastal Cathaysia Block of East Asia: Geodynamic implications. *International Geology Review*, 1–14. https://doi.org/10.1080/00206814.2022.2150899

Gao, P., Zheng, Y. F., & Zhao, Z. F. (2017). Triassic granites in South China: A geochemical perspective on their characteristics, petrogenesis, and tectonic significance. *Earth-Science Reviews*, *173*, 266–294. https://doi.org/10.1016/j.earscirev.2017.07.016

Gautheron, C., Tassan-Got, L., Barbarand, J., & Pagel, M. (2009). Effect of alpha-damage annealing on apatite (U–Th)/He thermochronology. *Chemical Geology*, *266*(3–4), 157–170. https://doi.org/10.1016/j.chemgeo.2009.06.001

Gilder, S., Gill, J., Coe, R., Zhao, X., Liu, Z., Wang, G., et al. (1996). Isotopic and paleomagnetic constraints on the Mesozoic tectonic evolution of South China. *Journal of Geophysical Research*, *1011*(B7), 16137–16154. https://doi.org/10.1029/96JB00662

Guenthner, W., Reiners, P., Ketcham, R., Nasdala, L., & Giester, G. (2013). Helium diffusion in natural zircon: Radiation damage, anisotropy, and the interpretation of zircon (U-Th)/He thermochronology. *American Journal of Science*, *313*(3), 145–198. https://doi.org/10.2475/03.2013.01

Gvirtzman, Z., & Nur, A. (1999). Plate detachment, asthenosphere upwelling, and topography across subduction zones. *Geology*, *27*(6), 563. https://doi.org/10.1130/0091-7613(1999)027<0563:PDAUAT>2.3.CO

Hames, W., & Bowring, S. A. (1994). An empirical study of the Argon diffusion geometry in muscovite. *Earth and Planetary Science Letters*, *124*(1–4), 161–169. https://doi.org/10.1016/0012-821X(94)00079-4

He, L., Sun, X., Li, P., Ai, S., & Li, J. (2021). Lithospheric structure near Jiuyishan, south China: Implications for asthenospheric upwelling and lithospheric modification. *Geophysical Research Letters*, *48*(24). https://doi.org/10.1029/2021GL096572

Hsü, K., Shu, S., Jiliang, L., Haihong, C., Haipo, P., & Sengor, A. M. C. (1988). Mesozoic overthrust tectonics in South China. *Geology*, *16*, 2. https://doi.org/10.1130/0091-7613(1988)016<0418:MOTISC>2.3.CO;2

Huang, H. Q., Li, X. H., Li, W. X., & Li, Z. X. (2011). Formation of high 18O fayalite-bearing A-type granite by high-temperature melting of granulitic metasedimentary rocks, southern China. *Geology*, *39*(10), 903–906. https://doi.org/10.1130/G32080.1

Jacob, J. B., & Moyen, J. F. (2021). Encyclopedia of geology (second edition). In D. Alderton, S. A. B. T. E. G. Eliasof, & E. Second (Eds.), *Granite and related rocks* (pp. 170–183). Academic Press.

Ji, W., Chen, Y., Chen, K., Lin, W., & Faure, M. (2018). Multiple emplacement and exhumation history of the Late Mesozoic Dayunshan-Mufushan Batholith in southeast China and its tectonic significance: 2. Magnetic fabrics and gravity survey. *Journal of Geophysical Research: Solid Earth*, *123*(1), 711–731. https://doi.org/10.1002/2017JB014598

Jiang, W. C., Li, H., Turner, S., Zhu, D. P., & Wang, C. (2020). Timing and origin of multi-stage magmatism and related W–Mo–Pb–Zn–Fe–Cu mineralization in the Huangshaping deposit, South China: An integrated zircon study. *Chemical Geology*, *552*, 119782. https://doi.org/10.1016/j.chemgeo.2020.119782

Jiang, Y. H., Jiang, S. Y., Dai, B. Z., Liao, S. Y., Zhao, K. D., & Ling, H. F. (2009). Middle to late Jurassic felsic and mafic magmatism in southern Hunan province, southeast China: Implications for a continental arc to rifting. *Lithos*, *107*(3–4), 185–204. https://doi.org/10.1016/j.lithos.2008.10.006

Jiang, Y. H., Wang, G. C., Liu, Z., Ni, C. Y., Long, Q., & Zhang, Q. (2015). Repeated slab advance–retreat of the Paleo-Pacific Plate underneath SE China. *International Geology Review*, *57*(4), 472–491. https://doi.org/10.1080/00206814.2015.1017775

Jolivet, M., Dominguez, S., Charreau, J., Chen, Y., Li, Y., Wang, Q., & Jolivet, C. (2010). Mesozoic and Cenozoic tectonic history of the Central Chinese Tian Shan: Reactivated tectonic structures and active deformation. *Tectonics*, *29*(6). https://doi.org/10.1029/2010TC002712

Kay, S., & Coira, B. (2009). Shallowing and steepening subduction zones, continental lithospheric loss, magmatism, and crustal flow under the Central Andean Altiplano-Puna Plateau. *Geological Society of America Memoir*, *204*, 229–259. https://doi.org/10.1130/2009.1204(11

Ketcham, R. (2005). Forward and inverse modeling of low-temperature thermochronometry data. *Reviews in Mineralogy and Geochemistry*, *58*(1), 275–314. https://doi.org/10.2138/rmg.2005.58.11

Kong, H., Li, H., Wu, Q. H., Xi, X. S., Dick, J. M., & GaboRatio, J. A. S. (2018). Co-development of Jurassic I-type and A-type granites in southern Hunan, South China: Dual control by plate subduction and intraplate mantle upwelling. *Geochemistry*, *78*(4), 500–520. https://doi.org/10.1016/j.chemer.2018.08.002

Li, C., Wang, Z., Lü, Q., Tan, Y., Li, L., & Tao, T. (2021). Mesozoic tectonic evolution of the eastern South China Block: A review on the synthesis of the regional deformation and magmatism. *Ore Geology Reviews*, *131*, 104028. https://doi.org/10.1016/j.oregeorev.2021.104028

Li, H., Wu, J. H., Evans, N. J., Jiang, W. C., & Zhou, Z. K. (2018). Zircon geochronology and geochemistry of the Xianghualing A-type granitic rocks: Insights into multi-stage Sn-polymetallic mineralization in South China. *Lithos*, *312–313*, 1–20. https://doi.org/10.1016/j.lithos.2018.05.001

Li, J., Shi, W., Zhang, Y., Dong, S., & Ma, Z. (2016). Thermal evolution of the Hengshan extensional dome in Central South China and its tectonic implications: New insights into low-angle detachment formation. *Gondwana Research*, *35*, 425–441. https://doi.org/10.1016/j.gr.2015.06.008

Li, J., Zhang, Y., Dong, S., & Johnston, S. T. (2014). Cretaceous tectonic evolution of South China: A preliminary synthesis. *Earth-Science Reviews*, *134*, 98–136. https://doi.org/10.1016/j.earscirev.2014.03.008

Li, J., Zhang, Y., Zhao, G., Johnston, S., Dong, S., Koppers, A., et al. (2017). New insights into Phanerozoic Tectonics of South China: Early Paleozoic sinistral and Triassic dextral transpression in the east Wuyishan and Chencai domains, NE Cathaysia. *Tectonics*, *36*(5), 819–853. https://doi.org/10.1002/2016TC004461

Li, J. H., Zhang, Y. Q., Dong, S. W., & Li, H. L. (2012). Late Mesozoic–early Cenozoic deformation history of the Yuanma Basin, Central South China. *Tectonophysics*, *570–571*, 163–183. https://doi.org/10.1016/j.tecto.2012.08.012

Li, S., Suo, Y., Li, X., Zhou, J., Santosh, M., Wang, P., et al. (2019). Mesozoic tectono-magmatic response in the East Asian ocean-continent connection zone to subduction of the Paleo-Pacific Plate. *Earth-Science Reviews*, *192*, 91–137. https://doi.org/10.1016/j.earscirev.2019.03.003

Li, X., & Zou, H. (2017). Late Cretaceous-Cenozoic exhumation of the southeastern margin of Coastal Mountains, SE China, revealed by fission-track thermochronology: Implications for the topographic evolution. *Solid Earth Sciences*, *2*(3), 79–88. https://doi.org/10.1016/j.sesci.2017.02.001

Li, Y., Dong, S., Zhang, Y., Li, J., Su, J., & Han, B. (2016). Episodic Mesozoic constructional events of Central South China: Constraints from lines of evidence of superimposed folds, fault kinematic analysis, and magma geochronology. *International Geology Review*, *58*(9), 1076–1107. https://doi.org/10.1080/00206814.2016.1146999

Li, Z. X., & Li, X. H. (2007). Formation of the 1300-km-wide intracontinental orogen and postorogenic magmatic province in Mesozoic South China: A flat-slab subduction model. *Geology*, *35*(2), 179–182. https://doi.org/10.1130/G23193A.1

Liu, J. X., Wang, S., Wang, X. L., Du, D. H., Xing, G. F., Fu, J. M., et al. (2020). Refining the spatio-temporal distributions of Mesozoic granitoids and volcanic rocks in SE China. *Journal of Asian Earth Sciences*, *201*, 104503. https://doi.org/10.1016/j.jseaes.2020.104503

Liu, Y., Lai, J. Q., Xiao, W. Z., Jeffrey, M. D., Du, R. J., Li, S. L., et al. (2019). Petrogenesis and mineralization significance of two-stage A-type granites in Jiuyishan, South China: Constraints from whole-rock geochemistry, mineral composition and zircon U-Pb-Hf isotopes. *Acta Geologica Sinica*, *93*(4), 874–900. https://doi.org/10.1111/1755-6724.13864

Lu, Y. F., Ma, L. Y., Qu, W. J., Mei, Y. P., & Chen, X. Q. (2006). U-Pb and Re-Os isotope geochronology of Baoshan Cu-Mo polymetallic ore deposit in Hunan province. *Acta Petrologica Sinica*, *22*, 2483–2492. (In Chinese with English abstract).

Mao, J. W., Cheng, Y. B., Maohong, C., & Pirajno, F. (2013). Major types and time–space distribution of Mesozoic ore deposits in South China and their geodynamic settings. *Mineralium Deposita*, *48*(3), 267–294. https://doi.org/10.1007/s00126-012-0446-z

Mao, J. W., Li, X. F., Wen, C., Lan, X. M., & Wei, S. L. (2004). Geological characteristics of the Furong Tin Orefield, Hunan, 40Ar-39Ar dating of tin ores and related granite and its geodynamic significance for rock and ore formation. *Acta Geologica Sinica - English Edition*, *78*, 481–491. https://doi.org/10.1111/j.1755-6724.2004.tb00158.x

Meng, L., Li, Z. X., Chen, H., Li, X. H., & Wang, X. C. (2012). Geochronological and geochemical results from Mesozoic basalts in southern South China Block support the flat-slab subduction model. *Lithos*, *132*(133), 127–140. https://doi.org/10.1016/j.lithos.2011.11.022

Murphy, J. B., Hynes, A., Johnston, S., & Keppie, J. (2003). Reconstructing the ancestral Yellowstone plume from accreted seamounts and its relationship to flat-slab subduction. *Tectonophysics*, *365*(1–4), 185–194. https://doi.org/10.1016/S0040-1951(03)00022-2

Qiu, L., Yan, D. P., Tang, S. L., Chen, F., Gong, L. X., & Zhang, Y. X. (2019). Cenozoic exhumation of the neoproterozoic sanfang batholith in South China. *Journal of the Geological Society*, *177*(2), 412–423. https://doi.org/10.1144/jgs2019-041

Reiners, P. W. (2005). Zircon (U-Th)/He thermochronometry. *Reviews in Mineralogy and Geochemistry*, *58*(1), 151–179. https://doi.org/10.2138/rmg.2005.58.6

Reiners, P. W., & Farley, K. A. (2001). Influence of crystal size on apatite (U–Th)/He thermochronology: An example from the Bighorn Mountains, Wyoming. *Earth and Planetary Science Letters*, *188*(3–4), 413–420. https://doi.org/10.1016/S0012-821X(01)00341-7

Reiners, P. W., Farley, K. A., & Hickes, H. J. (2002). He diffusion and (U–Th)/He thermochronometry of zircon: Initial results from Fish Canyon Tuff and Gold Butte. *Tectonophysics*, *349*(1–4), 297–308. https://doi.org/10.1016/S0040-1951(02)00058-6

Reiners, P. W., Spell, T., Nicolescu, S., & Zanetti, K. (2004). Zircon (U-Th)/He thermochronometry: He diffusion and comparisons with $^{40}Ar/^{39}Ar$ dating. *Geochimica et Cosmochimica Acta*, *68*(8), 1857–1887. https://doi.org/10.1016/j.gca.2003.10.021

Shi, H., Shi, X., Glasmacher, U. A., Yang, X., & Stockli, D. F. (2016). The evolution of eastern Sichuan basin, Yangtze block since Cretaceous: Constraints from low temperature thermochronology. *Journal of Asian Earth Sciences*, *116*, 208–221. https://doi.org/10.1016/j.jseaes.2015.11.008

Shi, W., Dong, S. W., Zhang, Y. Q., & Huang, S. Q. (2015). The typical large-scale superposed folds in the central South China: Implications for Mesozoic intracontinental deformation of the South China Block. *Tectonophysics*, *664*, 50–66. https://doi.org/10.1016/j.tecto.2015.08.039

Shi, X., Kohn, B., Yu, C., Tian, Y., Li, G., & Zhao, P. (2022). Thermo-tectonic history of coastal NW South China Sea: A low-temperature thermochronology study. *Tectonophysics*, *833*, 229344. https://doi.org/10.1016/j.tecto.2022.229344

Shu, L. S., Faure, M., Wang, B., Zhou, X., & Song, B. (2008). Late Palaeozoic–Early Mesozoic geological features of South China: Response to the Indosinian collision events in southeast Asia. *Comptes Rendus Geoscience*, *340*(2–3), 151–165. https://doi.org/10.1016/j.crte.2007.10.010

Shu, L. S., Jahn, B. M., Charvet, J., Santosh, M., Wang, B., Xu, X. S., & Jiang, S. Y. (2014). Early Paleozoic depositional environment and intraplate tectono-magmatism in the Cathaysia block (south China): Evidence from stratigraphic, structural, geochemical and geochronological investigations. *American Journal of Science*, *314*(1), 154–186. https://doi.org/10.2475/01.2014.05

Shu, L. S., Wang, B., Cawood, P., Santosh, M., & Xu, Z. (2015). Early Paleozoic and Early Mesozoic intraplate tectonic and magmatic events in the Cathaysia Block, South China. *Tectonics*, *34*(8), 1600–1621. https://doi.org/10.1002/2015TC003835

Shu, L. S., Zhou, X. M., Deng, P., Wang, B., Jiang, S. Y., Yu, J. H., & Zhao, X. X. (2009). Mesozoic tectonic evolution of the Southeast China Block: New insights from basin analysis. *Journal of Asian Earth Sciences*, *34*(3), 376–391. https://doi.org/10.1016/j.jseaes.2008.06.004

Shu, X. J., Wang, X. L., Sun, T., Xu, X., & Dai, M. N. (2011). Trace elements, U–Pb ages and Hf isotopes of zircons from Mesozoic granites in the Western Nanling Range, South China: Implications for petrogenesis and W–Sn mineralization. *Lithos*, *127*(3–4), 468–482. https://doi.org/10.1016/j.lithos.2011.09.019

Shuster, D. L., Flowers, R. M., & Farley, K. A. (2006). The influence of natural radiation damage on helium diffusion kinetics in apatite. *Earth and Planetary Science Letters*, *249*(3–4), 148–161. https://doi.org/10.1016/j.epsl.2006.07.028

Song, M., Shu, L., Santosh, M., & Li, J. (2015). Late Early Paleozoic and Early Mesozoic intracontinental orogeny in the South China Craton: Geochronological and geochemical evidence. *Lithos*, *232*, 360–374. https://doi.org/10.1016/j.lithos.2015.06.019

Su, J., Dong, S., Zhang, Y., Li, Y., Chen, X., Li, J., et al. (2017). Apatite fission track geochronology of the southern Hunan province across the Shi-Hang Belt: Insights into the Cenozoic dynamic topography of South China. *International Geology Review*, *59*(8), 981–995. https://doi.org/10.1080/00206814.2016.1240049

Sun, Y., Chen, Z., Boone, S. C., Zhong, F., & Tao, W. (2021). Exhumation history and preservation of the Changjiang uranium ore field, South China, revealed by (U-Th)/He and fission track thermochronology. *Ore Geology Reviews*, *133*, 104101. https://doi.org/10.1016/j.oregeorev.2021.104101

Suo, Y., Li, S., Jin, C., Zhang, Y., Zhou, J., Li, X., et al. (2019). Eastward tectonic migration and transition of the Jurassic-Cretaceous Andean-type continental margin along Southeast China. *Earth-Science Reviews*, *196*, 102884. https://doi.org/10.1016/j.earscirev.2019.102884

Suzuki, K., Shimizu, H., & Masuda, A. (1996). ReOs dating of molybdenites from ore deposits in Japan: Implication for the closure temperature of the ReOs system for molybdenite and the cooling history of molybdenum ore deposits. *Geochimica et Cosmochimica Acta*, *60*(16), 3151–3159. https://doi.org/10.1016/0016-7037(96)00164-0

Tang, S. L., Yan, D. P., Qiu, L., Gao, J. F., & Wang, C. L. (2014). Partitioning of the Cretaceous Pan-Yangtze Basin in the Central South China Block by exhumation of the Xuefeng Mountains during a transition from extensional to compressional tectonics? *Gondwana Research*, *25*(4), 1644–1659. https://doi.org/10.1016/j.gr.2013.06.014

Tao, N., Li, Z. X., Danišík, M., Evans, N. J., Batt, G. E., Li, W. X., et al. (2017). Thermochronological record of Middle–Late Jurassic magmatic reheating to Eocene rift-related rapid cooling in the SE South China Block. *Gondwana Research*, *46*, 191–203. https://doi.org/10.1016/j.gr.2017.03.003

Tao, N., Li, Z. X., Danišík, M., Evans, N. J., Li, R. X., Pang, C. J., et al. (2019). Post-250 Ma thermal evolution of the central Cathaysia Block (SE China) in response to flat-slab subduction at the proto-Western Pacific margin. *Gondwana Research*, *75*, 1–15. https://doi.org/10.1016/j.gr.2019.03.019

Vermeesch, P. (2008). Three new ways to calculate average (U–Th)/He ages. *Chemical Geology*, *249*(3–4), 339–347. https://doi.org/10.1016/j.chemgeo.2008.01.027

Vermeesch, P. (2010). HelioPlot, and the treatment of overdispersed (U–Th–Sm)/He data. *Chemical Geology*, *271*(3–4), 108–111. https://doi.org/10.1016/j.chemgeo.2010.01.002

Vermeesch, P. (2018). IsoplotR: A free and open toolbox for geochronology. *Geoscience Frontiers*, *9*(5), 1479–1493. https://doi.org/10.1016/j.gsf.2018.04.001

Vermeesch, P., & Tian, Y. (2014). Thermal history modelling: HeFTy vs. QTQt. *Earth-Science Reviews*, *139*, 279–290. https://doi.org/10.1016/j.earscirev.2014.09.010

Wang, B., Liangshu, S., Faure, M., Jahn, B., Lo, C. H., Charvet, J., & Liu, H. (2014). Phanerozoic multistage tectonic rejuvenation of the continental crust of the Cathaysia Block: Insights from structural investigations and combined zircon U-Pb and Mica 40Ar/39Ar geochronology of the granitoids in Southern Jiangxi Province. *The Journal of Geology*, *122*(3), 309–328. https://doi.org/10.1086/675664

Wang, F., Chen, H., Batt, G. E., Lin, X., Gong, J., Gong, G., et al. (2015). Tectonothermal history of the NE Jiangshan–Shaoxing suture zone: Evidence from $^{40}Ar/^{39}Ar$ and fission-track thermochronology in the Chencai region. *Precambrian Research*, *264*, 192–203. https://doi.org/10.1016/j.precamres.2015.04.009

Wang, X. Y., Suo, Y. H., Li, S. Z., Cao, X. Z., Li, X. Y., Zhou, J., et al. (2020b). Cenozoic uplift history and its dynamic mechanism along the eastern continental margin of South China. *Acta Petrologica Sinica*, *36*(6), 1803–1820. (in Chinese with English abstract). https://doi.org/10.18654/1000-0569/2020.06.10

Wang, Y., Fan, W., Guo, F., Peng, T., & Li, C. (2003). Geochemistry of Mesozoic mafic rocks adjacent to the Chenzhou-Linwu fault, South China: Implications for the lithospheric Boundary between the Yangtze and Cathaysia Blocks. *International Geology Review*, *45*(3), 263–286. https://doi.org/10.2747/0020-6814.45.3.263

Wang, Y., Fan, W., Zhang, G., & Zhang, Y. (2013). Phanerozoic tectonics of the South China Block: Key observations and controversies. *Gondwana Research*, *23*(4), 1273–1305. https://doi.org/10.1016/j.gr.2012.02.019

Wang, Y., Wang, Q., Deng, J., Xue, S., Li, C., & Ripley, E. M. (2021). Late Permian-Early Triassic mafic dikes in the southwestern margin of the South China block: Evidence for Paleo-Pacific subduction. *Lithos*, *384*, 105994. https://doi.org/10.1016/j.lithos.2021.105994

Wang, Y., Zhang, J., Zhang, B., & Zhao, H. (2018). Cenozoic exhumation history of South China: A case study from the Xuefeng Mt. Range. *Journal of Asian Earth Sciences*, *151*, 173–189. https://doi.org/10.1016/j.jseaes.2017.10.039

Wang, Y. J., Fan, W. M., Cawood, P. A., & Li, S. Z. (2008). Sr-Nd-Pb isotopic constraints on multiple mantle domains for Mesozoic mafic rocks beneath the South China Block hinterland. *Lithos*, *106*(3–4), 297–308. https://doi.org/10.1016/j.lithos.2008.07.019

Wang, Y. J., Wang, Y., Zhang, Y., Cawood, P. A., Qian, X., Gan, C., et al. (2021). Triassic two-stage intra-continental orogensis of the South China Block, driven by Paleotethyan closure and interactions with adjoining blocks. *Journal of Asian Earth Sciences*, *206*, 104648. https://doi.org/10.1016/j.jseaes.2020.104648

Wang, Y. J., Wang, Y. J., Li, S., Seagren, E., Zhang, Y., Zhang, P., & Qian, X. (2020). Exhumation and landscape evolution in eastern South China since the Cretaceous: New insights from fission-track thermochronology. *Journal of Asian Earth Sciences*, *191*, 104239. https://doi.org/10.1016/j.jseaes.2020.104239

Wei, W., Liu, C. Z., Hou, Y., Deng, C., Yan, W., Li, X. H., et al. (2021). Discovery of a Hidden Triassic arc in the southern South China Sea: Evidence for the Breakaway of a ribbon continent with implications for the evolution of the Western Pacific margin. *Terra Nova*, *34*(1), 12–19. https://doi.org/10.1111/ter.12556

Willett, C. D., Fox, M., & Shuster, D. L. (2017). A helium-based model for the effects of radiation damage annealing on helium diffusion kinetics in apatite. *Earth and Planetary Science Letters*, *477*, 195–204. https://doi.org/10.1016/j.epsl.2017.07.047

Willett, S., Herman, F., Fox, M., Stalder, N., Ehlers, T., Jiao, R., & Yang, R. (2021). Bias and error in modelling thermochronometric data: Resolving a potential increase in Plio-Pleistocene erosion rate. *Earth Surface Dynamics*, *9*(5), 1153–1221. https://doi.org/10.5194/esurf-9-1153-2021

Wolf, R. A., Farley, K. A., & Silver, L. T. (1996). Helium diffusion and low-temperature thermochronometry of apatite. *Geochimica et Cosmochimica Acta*, *60*(21), 4231–4240. https://doi.org/10.1016/S0016-7037(96)00192-5

Wu, J. H., Kong, H., Li, H., Algeo, T. J., Yonezu, K., Liu, B., et al. (2021). Multiple metal sources of coupled Cu-Sn deposits: Insights from the Tongshanling polymetallic deposit in the Nanling Range, South China. *Ore Geology Reviews*, *139*, 104521. https://doi.org/10.1016/j.oregeorev.2021.104521

Wu, J. H., Li, H., Algeo, T. J., Jiang, W. C., & Zhou, Z. K. (2018). Genesis of the Xianghualing Sn–Pb–Zn deposit, South China: A multi-method zircon study. *Ore Geology Reviews*, *102*, 220–239. https://doi.org/10.1016/j.oregeorev.2018.09.005

Wu, J. H., Li, H., Mathur, R., Bouvier, A., Powell, W., Yonezu, K., & Zhu, D. P. (2023). Compositional variation and Sn isotope fractionation of cassiterite during magmatic-hydrothermal processes. *Earth and Planetary Science Letters*, *613*, 118186. https://doi.org/10.1016/j.epsl.2023.118186

Xia, Y., Xu, X. S., & Zhu, K. Y. (2012). Paleoproterozoic S- and A-type granites in southwestern Zhejiang: Magmatism, metamorphism and implications for the crustal evolution of the cathaysia basement. *Precambrian Research*, *216–219*, 177–207. https://doi.org/10.1016/j.precamres.2012.07.001

Xu, X., Liang, C., & Xu, Y. (2021). Kinematic analysis of fault-slip data in the nanling tectonic Belt and Cretaceous to Paleogene tectonic evolution of the Central South China Block. *Journal of Asian Earth Sciences*, *221*, 104951. https://doi.org/10.1016/j.jseaes.2021.104951

Yan, D. P., Zhang, B., Zhou, M. F., Wei, G., Yuan, H. L., & Liu, S. (2009). Constraints on the depth, geometry and kinematics of Blind detachment faults provided by fault-propagation folds: An example from the Mesozoic fold belt of South China. *Journal of Structural Geology*, *31*(2), 150–162. https://doi.org/10.1016/j.jsg.2008.11.005

Yan, Y., Hu, X., Lin, G., Santosh, M., & Chan, L. S. (2011). Sedimentary provenance of the Hengyang and Mayang basins, SE China, and implications for the Mesozoic topographic change in South China Craton: Evidence from detrital zircon geochronology. *Journal of Asian Earth Sciences*, *41*(6), 494–503. https://doi.org/10.1016/j.jseaes.2011.03.012

Yao, J., Cawood, P. A., Shu, L., & Zhao, G. (2019). Jiangnan Orogen, South China: A ~970–820 Ma rodinia margin accretionary belt. *Earth-Science Reviews*, *196*, 102872. https://doi.org/10.1016/j.earscirev.2019.05.016

Yi, Y., Carter, A., Xia, B., Ge, L., Brichau, S., & Hu, X. Q. (2009). A fission-track and (U–Th)/He thermochronometric study of the northern margin of the South China Sea: An example of a complex passive margin. *Tectonophysics*, *474*(3–4), 584–594. https://doi.org/10.1016/j.tecto.2009.04.030

Yu, J. H., O'Reilly, S. Y., Zhou, M. F., Griffin, W. L., & Wang, L. (2012). U–Pb geochronology and Hf–Nd isotopic geochemistry of the Badu complex, southeastern China: Implications for the Precambrian crustal evolution and paleogeography of the Cathaysia block. *Precambrian Research*, *222–223*, 424–449. https://doi.org/10.1016/j.precamres.2011.07.014

Zhang, R. Q., Lu, J. J., Wang, R. C., Yang, P., Zhu, J. C., Yao, Y., et al. (2015). Constraints of in situ zircon and cassiterite U–Pb, molybdenite Re–Os and muscovite ^{40}Ar–^{39}Ar ages on multiple generations of granitic magmatism and related W–Sn mineralization in the Wangxianling area, Nanling Range, South China. *Ore Geology Reviews*, *65*, 1021–1042. https://doi.org/10.1016/j.oregeorev.2014.09.021

Zhang, Z., Ning, Y., Lu, Y., Cao, J., Fu, J., Zhao, Z., et al. (2021). Geological characteristics and metallogenic age of Tengshan'ao Sn deposit in Dayishan of South Hunan and its prospecting significance. *Solid Earth Sciences*, *6*(1), 37–49. https://doi.org/10.1016/j.sesci.2021.01.002

Zhao, P., Yuan, S., Mao, J., Santosh, M., Li, C., & Hou, K. (2016). Geochronological and petrogeochemical constraints on the skarn deposits in Tongshanling ore district, southern Hunan Province: Implications for Jurassic Cu and W metallogenic events in South China. *Ore Geology Reviews*, *78*, 120–137. https://doi.org/10.1016/j.oregeorev.2016.03.004

Zhao, P., Yuan, S., Mao, J., Yuan, Y., Zhao, H., Zhang, D., & Shuang, Y. (2018). Constraints on the timing and genetic link of the large-scale accumulation of proximal W–Sn–Mo–Bi and distal Pb–Zn–Ag mineralization of the world-class Dongpo orefield, Nanling Range, South China. *Ore Geology Reviews*, *95*, 1140–1160. https://doi.org/10.1016/j.oregeorev.2017.12.005

Zhou, X. M., & Li, W. X. (2000). Origin of late Mesozoic igneous rocks in southeastern China: Implications for lithosphere subduction and underplating of mafic magmas. *Tectonophysics*, *326*(3), 269–287. https://doi.org/10.1016/S0040-1951(00)00120-7

Zhou, X. M., Shen, W. Z., Shu, L. S., & Niu, Y. L. (2006). Petrogenesis of Mesozoic granitoids and volcanic rocks in South China: A response to tectonic evolution. *Episodes*, *29*(1), 26–33. https://doi.org/10.18814/epiiugs/2006/v29i1/004

Zhu, J., Wang, R., Zhang, P., Xie, C., Zhang, W., Zhao, K., et al. (2009). Zircon U-Pb geochronological framework of Qitianling granite batholith, middle part of Nanling Range, South China. *Science in China - Series D: Earth Sciences*, *52*(9), 1279–1294. https://doi.org/10.1007/s11430-009-0154-4